Retroreflective Background Oriented Schlieren Imaging Results from the NASA Plume/Shock Interaction Test

Nathanial T. Smith[*]
ACI/NASA Ames Research Center, Moffett Field, CA 94035, USA

Donald A. Durston[†], James T. Heineck[‡]
NASA Ames Research Center, Moffett Field, CA 94035, USA

In support of NASA's Commercial Supersonics Technology (CST) project, a test was conducted in the 9-by-7 ft. supersonic section of the NASA Ames Unitary Plan Wind Tunnel (UPWT). The tests were designed to study the interaction of shocks with a supersonic jet characteristic of those that may occur on a commercial supersonic aircraft. Multiple shock generating geometries were tested to examine the interaction dynamics as they pertain to sonic boom mitigation. An integral part of the analyses of these interactions are the interpretation of the data generated from the retroreflective Background Oriented Schlieren (RBOS) imaging technique employed for this test. The regularization-based optical flow methodology used to generate these data is described. Sample esults are compared to those using normalized cross-correlation. The reduced noise, additional feature detail, and fewer false artifacts provided by the optical flow technique produced clearer time-averaged images, allowing for better interpretation of the underlying flow phenomena. These images, coupled with pressure signatures in the near field, are used to provide an overview of the detailed interaction flowfields.

Nomenclature

I = intensity image
LE = leading edge
M = freestream Mach no.
NPR = nozzle pressure ratio
P_{NT} = nozzle total pressure
TE = trailing edge
u = horizontal pixel displacement (pixel velocity)
v = vertical pixel displacement (pixel velocity)
x, y = image coordinates
$\mathbf{V}$ = vector pixel displacement
α = angle of attack
κ = smoothing parameter for regularization
Ω = image domain

I. Introduction

The Commercial Supersonics Technology (CST) project at NASA is focused on developing technologies for future supersonic commercial aircraft, including the study of sonic boom reduction. Ongoing research

---

[*] Research Engineer, ACI/Experimental Aero-Physics Branch, M/S 260-1, Member AIAA.
[†] Aerospace Engineer, Experimental Aero-Physics Branch, M/S 260-1, Member AIAA.
[‡] Photographic Technologist, Experimental Aero-Physics Branch, M/S 260-1, Member AIAA.

in conjunction with industry partners is focused on integrated airframe configurations that lower the sonic boom of the aircraft with the goal of enabling supersonic flight through commercial airspace. Computational studies are able to predict shocks and their associated pressure signatures generated from the "low boom" aircraft forebody with confidence; yet difficulties are still encountered with modeling the shocks from the aft portion of the vehicle. This is due to the complex flow caused by the interaction of the supersonic nozzle exhaust with shocks generated by structures on the aft section of the airframe (*e.g.* tails or nozzle shielding) designed to reduce the pressure signature.

A test was recently conducted at the 9-by-7 ft. Supersonic Wind Tunnel (SWT) of the NASA Ames Unitary Plan Wind Tunnel (UPWT) to study the effects of supersonic nozzle plume/shock interactions that are likely to occur on the aft portion of a reduced sonic boom commercial aircraft. A simplified generic wind tunnel model was designed to generate plume/shock interactions representative of those that can occur on low boom aircraft. Cliff *et al.* performed detailed computational studies that guided the design of the experiment and shock-generating geometries.[?] The primary goals of the test were to assess these shock interactions with the nozzle plume through schlieren image acquisition and measurement of the pressure signature in the near field. Multiple shock generating bodies were used to create flow structures typical of those on the aft portion of a commercial supersonic aircraft designed to quiet sonic boom. The high quality data provided by these tests is designed to assist prediction studies of the aft portion of the aircraft to assess the reduced pressure signatures.

The work of this paper presents the background oriented schlieren (BOS) images of the plume/shock interactions of select model configurations. Whereas the creation of BOS images typically utilizes cross-correlation methods similar to those used in particle image velocimetry, this work uses optical flow to construct visualizations of the density gradients. Select schlieren images processed using optical flow and cross-correlation are compared, and it is demonstrated that the use of optical flow produces results with greater detail. These schlieren images, coupled with near field pressure signature data significantly aid the interpretation of the plume/shock interaction flowfields. The primary goal of this paper is to provide an overview of the detailed interaction flowfields and their trends revealed by the detailed schlieren images to assist computational validation studies in their prediction efforts.

II. Test Overview

Durston *et al.*,[1] of which this paper is a companion, provides a thorough description of the plume/shock interaction experiment. The 9-by 7-ft Supersonic Wind Tunnel (SWT) at NASA Ames Research Center is a continuous run variable Mach number wind tunnel with an asymmetric sliding nozzle block which allows freestream Mach numbers between 1.5 and 2.5. The tunnel operates at Reynolds numbers between .8 and 5.7x10^6/ft., and is capable of freestream total pressures between 634 and 3600 psfa.[2]

A total of four shock-generating geometries with shocks interacting with a high pressure nozzle plume were tested. The high-pressure nozzle was designed to have an ideal expansion at a Nozzle Pressure Ratio (NPR) of 8 with a nominal exit Mach number of 2. Three tail configurations were used: a double wedge geometry, a biconvex tail, and a NASA Langley Research Center tail configuration termed 25-D. In addition, an aft-deck configuration that approximates the effect of nozzle shielding was tested. These shock-generating models are discussed in more detail as their results are presented. Tests were conducted with all shock generating models at nozzle off ($NPR = 1$), over-expansion ($NPR = 4$), ideal expansion ($NPR = 8$), and under-expansion ($NPR = 14$ and higher). Data were acquired for all configurations at various angles of attack α, and at freestream Mach numbers of 1.6 and 2 and a Reynolds number of approximately 3.5x10^6/ft. The results presented here focus on three configurations: the biconvex tail, the 25-D tail, and the aft-deck. Schlieren images are presented for varying freestream Mach number and angle of attack, along with their select associated pressure signatures from the near field.

Figure 1 on the following page shows the model as installed in the 9x7 SWT at the NASA Ames UPWT. The model is shown configured with the 25-D tail shock generator. Both the high pressure nozzle and shock generator are attached to the model blade strut (also shown). The pressure rail used to measure shock configuration signatures can be seen mounted a window blank in the north wall of the test section. The speckled background pattern used for schlieren imaging is located below the pressure rail. Note the pressure rail is mounted on the window blank replacing the schlieren window, necessitating the use of a background oriented schlieren measurement technique for these experiments.

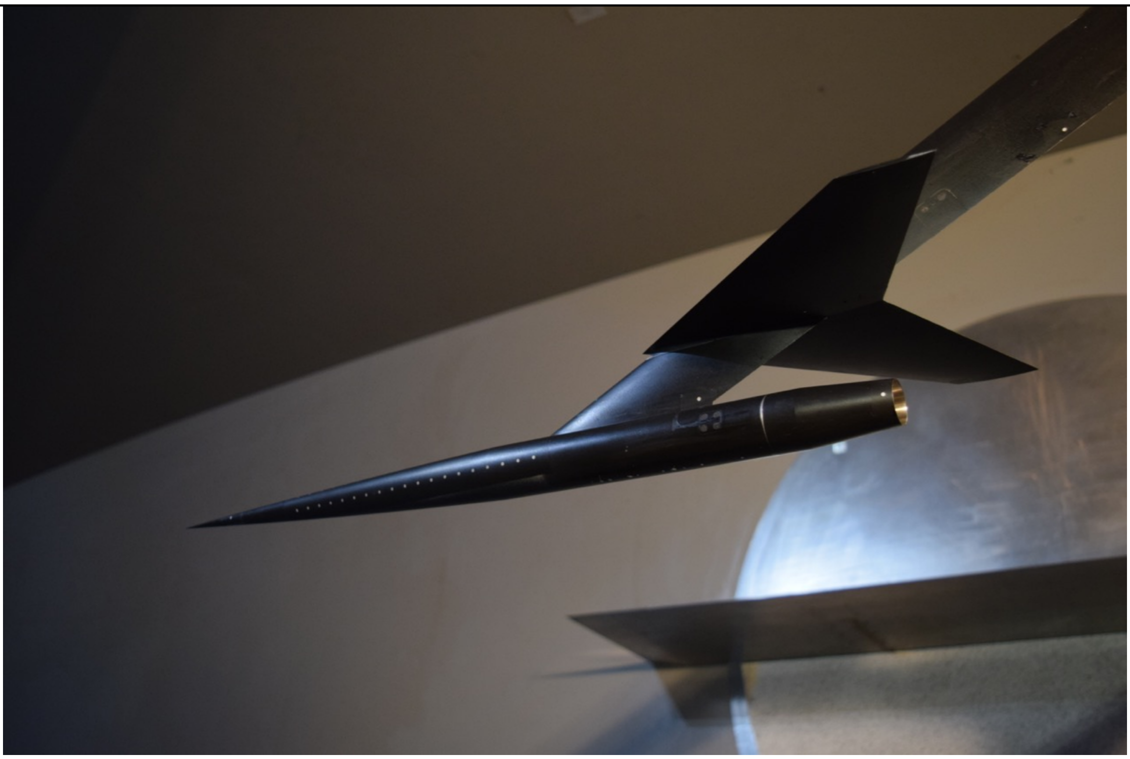

Figure 1. The plume/shock interaction model as installed in the NASA Ames 9x7 SWT. Note the background pattern on the tunnel wall below the pressure rail.

III. Background Oriented Schlieren

Traditional schlieren imaging relies on careful mirror placement and a knife edge placed between the illumination source and the test section to emphasize the horizontal or vertical gradients of density, depending on the orientation of the knife edge. Background oriented schlieren (BOS) imaging has seen increasingly wide spread use due to its versatility and relative ease of setup as opposed to a classical schlieren system. There is no need for a mirror system or knife edge; only a suitable background, camera and illumination source are required. The technique can be used where traditional schlieren cannot as only a single optical access window is needed. Unlike conventional schlieren, both horizontal and vertical density gradients can be detected from the same experiment. First detailed by Dalziel, Hughes, and Sutherland[3] and termed "synthetic schlieren", BOS relies the visualization of a random speckle background pattern shifted by the presence of a density gradient as compared to a quiescent background. Richard and Raffel[4] expanded upon the technique, applying it to wind tunnel and full scale-flight experiments. A thorough overview of BOS techniques and applications is provided by Raffel.[5]

A description of the BOS technique is shown in figure 2 on the next page. A light ray passes through a density gradient and deflects, causing a distortion in the wind-on background pattern relative to the background pattern at wind-off conditions. The deflection of the light ray is directly proportional to the density gradient. The shift of the distorted background pattern relative to the reference image is typically detected using normalized cross-correlation. Sub-pixel localization is accomplished by identifying peaks in the correlation map. These detected shifts in the x and y directions are mapped to grayscale intensity values to create the schlieren image in either the vertical or horizontal knife-edges to render the dx or dy gradients respectively.

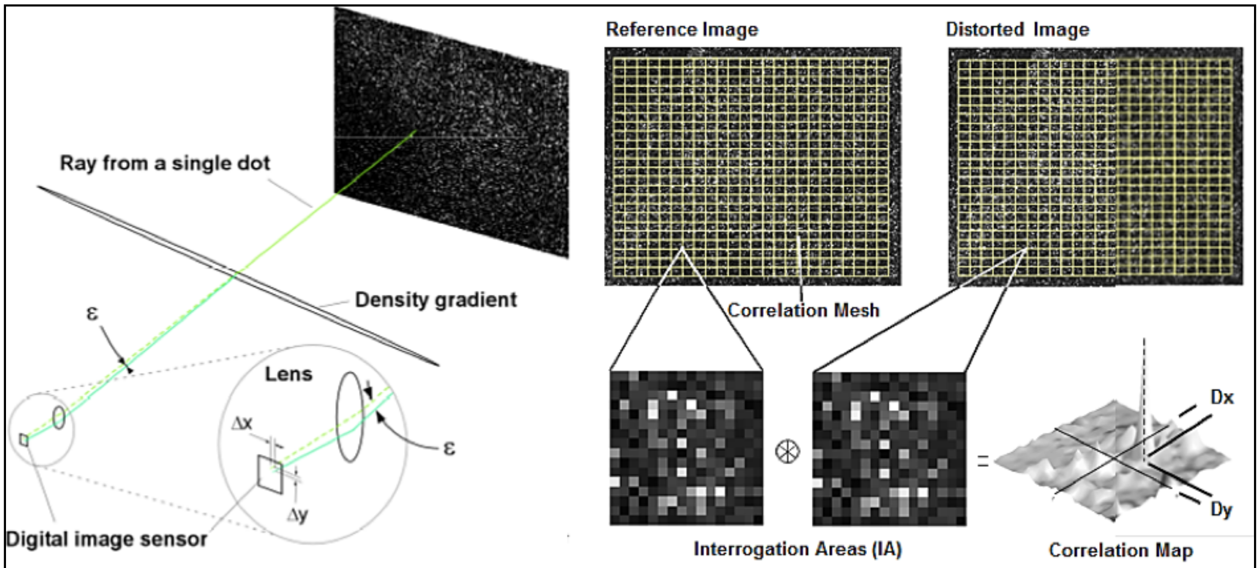

Figure 2. Illustration of the background oriented schlieren technique.

IV. Schlieren System Configuration

The Retroreflective Background Oriented Schlieren (RBOS) imaging technique was used to acquire all schlieren images for this test. The use of a window blank for mounting the pressure rail on the tunnel side wall (see figure 1 on the preceding page) rendered traditional schlieren imaging impossible. The retroreflective BOS technique developed by Heineck *et al.*[6] uses a random speckle background pattern that has been applied to an adhesive retroreflective material. The retroreflective background pattern is shown in figure 1 on the previous page, mounted below the pressure rail on the bottom portion of the window blank that replaces the schlieren window. The RBOS technique can be advantageous for two reasons: first, the background material allows for more efficient use of the illumination source, and secondly, when optical access and spatial constraints are limited in the experiment, the system allows for a simplified setup. In this test the method was particularly useful as multiple optical measurement techniques were employed, which required placement of multiple cameras and illumination sources. Figure 3 on the following page is a schematic of the schlieren system used in this test. The cameras used for the recording of the reference and data images were Imperx B6620 29 megapixel cameras. The pixel pitch is 4.7 microns and the array dimension is 6576x4384. It operates at approximately 2 Hz. The camera was fitted with a Zeiss ZF 85 mm lens set to f22. Due to the specific technique used to create the schlieren images in this test (discussed in the following section), it was desired to eliminate as many hard shadows as possible in the raw images. A diffuse ring illumination source was therefore used to mitigate shadows, and had a pulse duration of approximately 100 μs. To acquire the schlieren data, the model blade strut was rotated out of a position parallel to the pressure rail for placement parallel to the background.

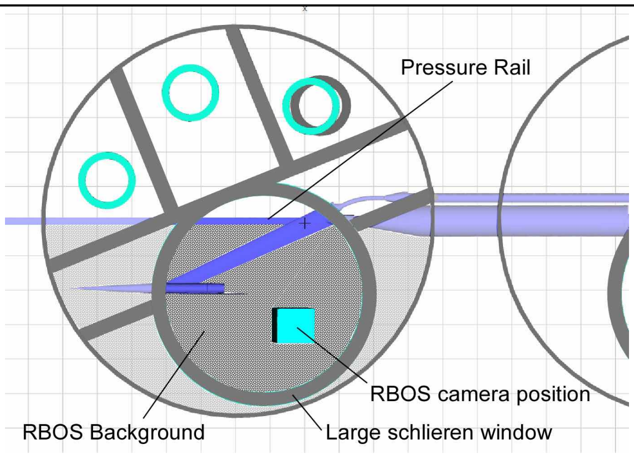

Figure 3. Diagram of the plume/shock RBOS system configuration.

V. Data Reduction Methodology

Optical flow, or the apparent motion between images due to changes in brightness, is an established technique in the computer vision community for motion estimation in image pairs and video. The global regularization-based method of Horn and Schunck[7] is used here due to its ability to solve the flowfield at all image points, its intuitive mathematical form to those with a fluid dynamics background, and the performance of the method the authors have found across multiple data sets. Optical flow assumes that the brightness of a pixel (or object) remains constant between frames, and that the motion between frames is small. This can be written as

$$I\left(x,y,t\right)\approx I\left(x+\delta x,\delta y+y,t+\delta t\right) \tag{1}$$

or

$$\nabla I\cdot\mathbf{V}+I_t=0 \tag{2}$$

where $\mathbf{V}=(u,v)$ is the pixel displacement (or "brightness velocity") between frames, and the subscript t denotes the image temporal derivative. Equation (2) is called the brightness constraint equation, and its solution requires an additional mathematical constraint. Horn and Schunck suggest the $L2$ norm of the velocity gradients as a smoothing function. The problem then becomes the minimization of the functional containing the data term (equation (2)), and the $L2$-based regularizer (or smoothing term), over the image domain Ω. The functional is given in equation (3) below

$$E=\int_{\Omega}\{(\nabla I\cdot\mathbf{V}+I_t)^2+\kappa^2\left(\|\nabla u\|^2+\|\nabla v\|^2\right)\}d\Omega \tag{3}$$

The data term in equation (3) is given a quadratic penalty as proposed in,[7] and the smoothness constraint is weighted by the free parameter κ. Using the Euler-Lagrange equation, and an approximation to the resulting Laplacian terms of u and v as in[7] yields the following system of equations:

$$\begin{aligned} u &= \bar{u}-I_x\frac{I_x\bar{u}+I_y\bar{v}+I_t}{\kappa^2+I_x^2+I_y^2} \\ v &= \bar{v}-I_y\frac{I_x\bar{u}+I_y\bar{v}+I_t}{\kappa^2+I_x^2+I_y^2} \end{aligned} \tag{4}$$

The terms u and $\bar{u}$ result from the separation of the center and off-diagonal terms of the numerical approximation to the Laplacian of u, respectively (likewise for v and $\bar{v}$). Subscripts denotethe spatial and temporal derivatives of the images.

The system given in equations (4) is an iterative scheme which may be solved by either a Jacobi or Gauss-Seidel method. The former has been implemented as it lends itself to straightforward parallelization. The optical flow calculations were performed using an in house code developed at the Fluid Mechanics Laboratory at NASA Ames, written in C++ and uses the OpenCV computer vision libraries. The existing implementation of Horn-Schunck in OpenCV was not used, as it is sufficient for approximation as desired in typicalcomputer vision applications, but has limitations in its numerical implementation making it poorly suited when accuracy and convergence criterion are more strict.

VI. Results

All reference images were taken with the model installed in the test section. Due to the additional lighting considerations for optical flow data reduction imposed by the brightness constraint in equation (2), it was desired to capture the model shadow in the background as it appears in wind-on images. This helps to mitigate regions in the image pairs where the brightness constancy assumption may fail, yielding an area that may not be solvable by optical flow. Note that these additional considerations due not apply when using image cross-correlation techniques. A typical wind-off (reference) wind-on (flow) image pair from the raw data set is shown in figure 4 below for the 25-D model test case. The shadows cast by the sting assembly and model are contained in both images, and have been mitigated to some degree by the diffuse ring lighting source. Close examination of figures 4(a) and 4(b) show that there has been slight motion of the model between frames. This is due to the rotation of the blade strut during the test, and will be discussed further as it pertains to results.

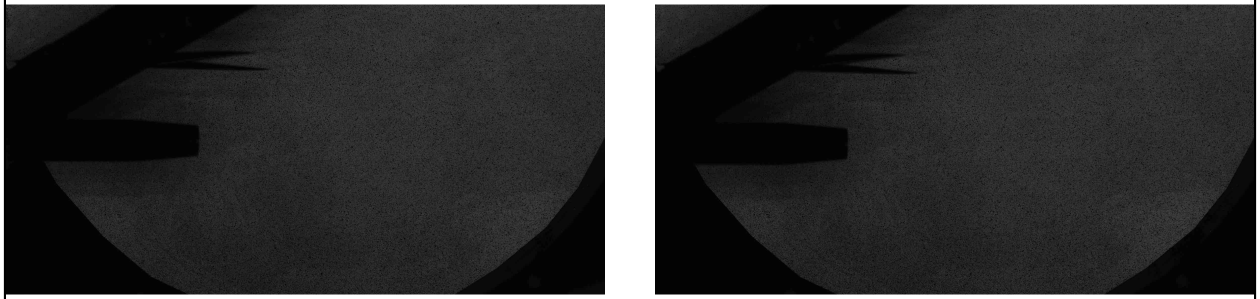

(a) Wind-off reference image.

(b) Wind-on flow image.

Figure 4. Raw RBOS data pair sample. Shadows are present in both wind-off and wind-on conditions.

All image displacement calculations were performed against a single static wind-off reference image. Wind-on images were registered to the background to account for camera motion or vibration using a projective transformation. The projective transform allows correction of any translation, rotation or titling of the camera relative to the wind-off position during image acquisition. This registration step is important in both cross-correlation and optical flow methods to calculate accurate displacements caused by density gradients. Each schlieren image shown in the following sections is an average of 20 instantaneous images. The purpose of image time-averaging is to eliminate many of the unsteady compression and Mach waves (and their reflections) that occur in the test section.

A. Sample Comparison with Cross-correlation

Figure 5 on the following page shows instantaneous (non time-averaged) images for two test cases. Schlieren images obtained from normalized cross-correlation and optical flow methods are presented side by side for the same time instance. It is immediately clear that the optical flow images in figures 5(b) on the next page and 5(d) on the following page provide much greater detail than their cross-correlation counterparts in figures 5(a) on the next page and 5(c) on the following page. The interaction details of both the aft-deck and 25-D models are more apparent, and additional compression waves in the test section are revealed in the optical flow calculations. Close examination of figures 5(b) on the next page and 5(d) on the following page reveal that the optical flow calculations have small symmetric noise bands above and below the nozzle, and to a lesser extent near the shock generating model. This is due to the presence of shadows in the raw images; these shadows create an effective occlusion of the background pattern that violates the brightness constancy constrain in equation (2). This creates a small region in the image that cannot be solved by optical flow. These same noise bands are not evident in the cross-correlation results, as these methods are much less sensitive to changes in brightness. In this specific case, the locations of the shadows do not obscure any of the interaction flow phenomena.

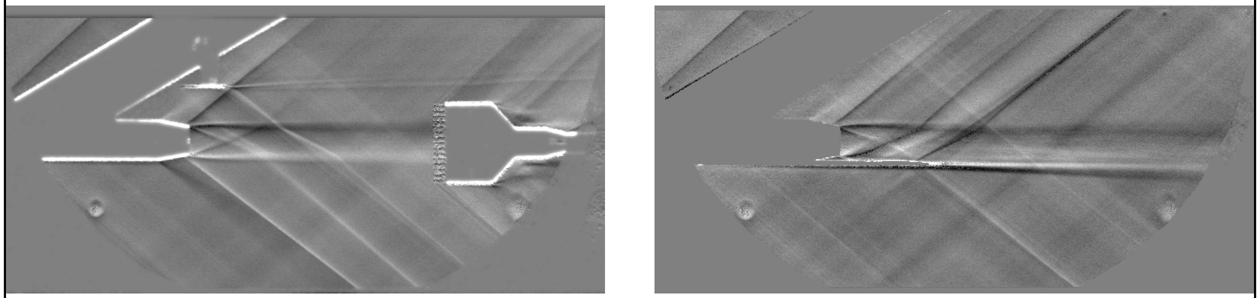

(a) Aft-deck cross-correlation solution.

(b) Aft-deck optical flow solution.

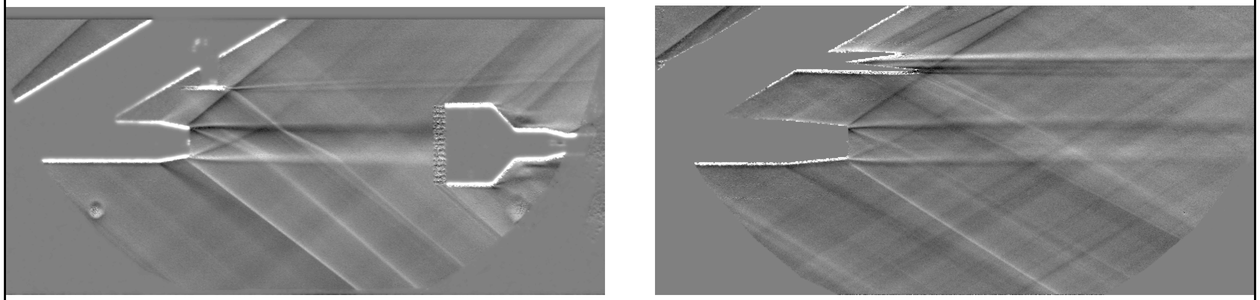

(c) 25-D cross-correlation solution.

(d) 25-D optical flow solution.

Figure 5. Comparison of instantaneous schlieren images using cross-correlation and optical flow for the aft-deck and 25-D configurations.

B. Biconvex Tail Interaction

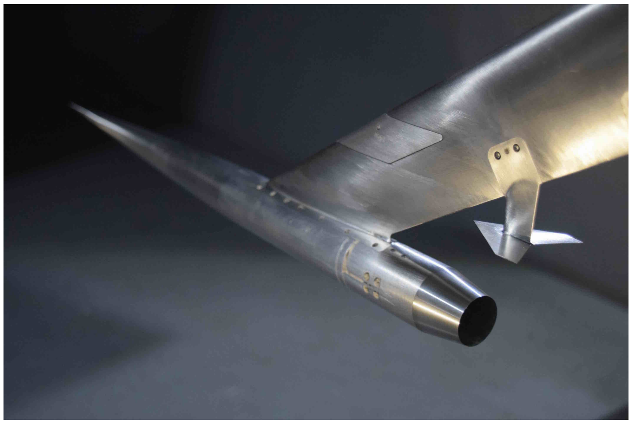

Figure 6. The biconvex tail model installed in the test section.

Figure 6 shows the biconvex tail shock-generating model mounted above the nozzle on the model blade strut. The tail was modeled after a low-boom-wing-tail designed at NASA Ames in the 1990's.[8] The model has a root chord of 1.5 in. and has a 1.8 in. span. The leading and trailing edge sweeps are 58° and 27° respectively. Schlieren images were acquired for the biconvex tail configuration at freestream Mach numbers of 1.6 and 2 with a Reynolds number of 3.5x10^6/ft., at angles of attack α of 0° for both Mach numbers, and 1° at the Mach 2 condition, all with NPR sweeps. Results for varying NPR at zero angle of attack α at Mach 2 and 1.6 are presented here, as well as for $\alpha = 1°$ at the Mach 2 case. This was the highest angle of attack of the model that could still be viewed by the BOS imaging system. Pressure signature plots are presented for the zero angle of attack test cases, with the model located 8 in. from the pressure rail. During these runs there appeared to be slight vibration of the entire model/strut assembly, although due to the small size of the biconvex tail, it is difficult to tell if this had any effect on the location of the shock-generating structure from viewing the raw sequence.

1. *The Biconvex Tail $M = 2$ Interaction*

Results of the biconvex tail plume/shock interaction at a freestream Mach number of 2 and 0° angle of attack are presented in figure 7 on page 11, at nozzle pressure ratios NPR of 4, 8, and 14, increasing from top. As compared to the instantaneous images, characteristic of figure 5 on the previous page, many of the unsteady compression waves have been removed by the time-averaging of 20 images. The leading an trailing edge (LE and TE) shocks from the tail, as well as the wake from the trailing edge are seen clearly at all values of NPR. As expected, the structures immediately near the model are unchanged with nozzle operating regime. At no NPR do the shocks from the outer nozzle lip impinge on the tail. The leading and trailing edge shocks from the shock generator steepen as they pass through the nozzle plume. This steepening through the nozzle plume becomes more pronounced with increasing NPR, and hence plume Mach number.

Figure 7(a) on page 11 shows the nozzle operating in the over-expanded regime. Symmetric expansion fans from the nozzle boat tail and outer lip are evident. A pair of shocks emanate from the inner lip of the nozzle to equilibrate the exit pressure and form a Mach disk at their intersection. These oblique shocks inside the nozzle core flow partially transmit through and partially reflect from the free boundary as series of weak expansion fans. There is faint evidence of a second normal shock just downstream of the first. This was confirmed by viewing the dx schlieren images (not shown). The shock diamond patterns have dissipated approximately one nozzle diameter downstream of the exit plane. An examination of the instantaneous images indicated a slight unsteadiness of the shock diamond structures. The transmitted nozzle inner lip shocks turn the jet parallel to the tunnel wall. These shocks emanating from the inner nozzle lip coalesce with the nozzle outer lip expansion immediately away from the nozzle core. The shocks generated by the biconvex tail should largely be encapsulated by the plume as the tail span is on the order of the nozzle diameter. The TE shock appears to steepen as it passes through the plume and turns the plume slightly. There is not strong enough image evidence to say the same of the LE shock – although this may be due to the fact that the blade strut prevents a strong LE shock from forming. The expansion wave from the convex surface should impinge on the plume boundary, reflecting as compression waves, yet there is little evidence of the upper shear layer deflection to substantiate this.

The nozzle was designed to be ideally expanded at an NPR of 8. This on-design operation of the nozzle in figure 7(b) on page 11 shows a minor contraction at the nozzle exit plane, suggesting a slight over-expansion. The shock diamond pattern dissipates approximately one nozzle diameter downstream of the exit plane, and the flow is turned parallel to the nozzle by the pair of inner nozzle lip shocks. Both the LE and TE shocks from the tail again steepen as they pass through the plume, and to a slightly greater degree from the over-expanded case in figure 7(a) on page 11 due to the increased plume Mach number. There seems to be more evidence of the expansion fan from the lower tail convex surface impinging on the upper shear layer and slightly turning the flow. The plume is turned back by the tail TE shock. The nozzle outer lip shock has steepened with increased plume Mach number, having shifted upstream at the point where it terminates in the lower portion of the image, and does not coalesce in the immediate near field with the nozzle inner lip (transmitted) shock from inside the plume.

Figure 7(c) on page 11 shows the interaction with the under-expanded nozzle plume at an NPR of 14. Note the bulging of the plume due to under-expansion. Expansion fans emanate from the nozzle inner lip, decreasing the plume pressure. The expansion pattern persists for approximately two nozzle diameters from the exit plane. Both the leading and trailing edge shocks from the biconvex tail steepen through the plume, and turn again as they pass through the lower jet boundary. The tail shocks passing through the plume are steepened most here, as the exit Mach number is highest. The effects of the expansion fan from the tail impinging on the upper shear layer appear most clear at this NPR, where a portion of the plume becomes briefly concave. The outer nozzle lip shock has steepened further as compared to the on-design condition, yet there is no longer a transmitted (inner nozzle lip) shock from the plume since the flow is now under-expanded.

In summary, it is apparent the interaction length scale in the near field, defined here as the distance between the nozzle outer lip shock and the tail trailing edge shock, increases with NPR, largely due to the steepening of the outer nozzle lip shock with NPR. Of note is the fact that the tail model shock and expansion waves do not cause any significant deflection of the nozzle plume. The shocks from the nozzle do not seem to effect the flow around the biconvex tail, at least at a resolution that can be observed in the images – *e.g.* there is no deflection of the wake.

2. *Biconvex tail $M = 1.6$ Interaction: Effects of freestream Mach number*

The biconvex tail plume/shock interactions at a reduced freestream Mach number of 1.6 are shown in figure 8 on page 12, where NPR is again increasing from top. The exit pressure rake was used during the image acquisition, although this should not effect the upstream flow structures. The gross features of the shock generating body and nozzle aft-section (such as the tail wake and nozzle lip shocks) evident in figure 7 on page 11 remain largely unchanged. Note that the tail leading and trailing edge shocks have steepened with decreased freestream Mach number as expected; the same holds for the nozzle lip shocks. These shocks again steepen further with increasing plume exit Mach number (NPR). As the leading and trailing edge shocks from the shock-generating body pass through the plume, they decrease in wave angle (again with NPR) from their Mach 2 freestream counterparts in figure 7 on page 11. This is due to the larger difference in Mach number between the freestream and the plume with the reduced freestream Mach number. All shock structures below the plume have shifted upstream with all NPR values at the lower freestream Mach number. The transmitted tail shocks have moved upstream with decreasing freestream Mach numbers at all values of NPR. These tail LE and TE shocks transmitted through the plume move further downstream with increasing NPR. This is due to the increased steepening of these shocks, which changes the geometry of transmission point as they pass through the plume with increased plume Mach number. Note that for the under-expanded nozzle, the upper nozzle lip shock nearly impinges the biconvex trailing edge surface. For all values of NPR, the biconvex tail wake is deflected by the exit pressure rake. The interaction length scale again increases with NPR. It is difficult to determine from the image evidence alone if the interaction length scales change with freestream Mach number

3. *Biconvex Tail $M = 2$, $\alpha = 1°$ Interaction: Effects of angle of attack*

The schlieren images from the biconvex tail-interaction at 1° and a freestream Mach number of 2 are shown in figure 9 on page 13. There appears to be no appreciable difference in the near field of any of the flow structures from the zero degree angle of attack case shown in figure 7 on page 11. The interaction length scales appear slightly smaller, but this is due only to the increased viewing area away from the model with increased α. At such a small angle of attack, and lacking pressure signature data for this values of α, there are no significant conclusions that can be drawn from this case. Pressure signature data is available at higher values of α and are discussed in reference.[1]

4. *Pressure signatures*

Near field pressure signatures are provided in figure 10 on page 14 for freestream Mach numbers of 2 and 1.6 for zero angle of attack, and correspond to figures 7 on the following page and 8 on page 12. These signatures were taken with a model distance from the pressure rail of approximately 8 in., and each figure plots the normalized pressure signature for varying NPR. The most upstream portion of the signatures associated with the nose shock and nozzle body expansion, as well the additional shock associated with the model blade strut are labeled in figures 10(a) on page 14 and 10(b) on page 14. These structures remain unchanged with NPR as expected, and retain their shape for both freestream Mach numbers. The largest decrease in pressure in both figures extends to approximately $x/L \approx 1^+$, for the lowest NPR of 4 for both freestream Mach numbers, and is caused by the expansion fan emanating from the nozzle boat tail. The effect of the outer nozzle lip shock is clearly seen at the end of the expansion, and is the largest overall pressure rise in the signature. This shock, as concluded from the images, increases in strength with increasing NPR and moves downstream. For the over-expanded cases, the effect of the transmitted expansion wave is shown at approximately $x/L \approx 1$ as a drop in pressure for the Mach 2 and 1.6 cases in figure 10(a) on page 14 and 10(b) on page 14 respectively. The tail LE shock was difficult to view at the lower NPR values of 4 and 8 for both cases, and appears to be smeared in the signature near $x/L \approx 1.1$ in both instances. When the nozzle is under-expanded, the effect of the LE shock is more clear − and located just downstream of the transmitted expansion wave. The final pressure drop in each figure is caused by the expansion from the lower surface of the biconvex tail. The tail trailing edge shock, located near $x/L \approx 1.2$ in both figures, moves downstream with increasing NPR for both Mach numbers. The pressure signatures also confirm that the interaction length scale increases with NPR regardless of freestream Mach number. Although it was difficult to tell if the overall length scale varied with freestream Mach number (at fixed NPR) from viewing the images, it would appear from figures 10(a) on page 14 and 10(a) on page 14 that the interaction scale is slightly smaller in the Mach 1.6 case, at least in the near field.

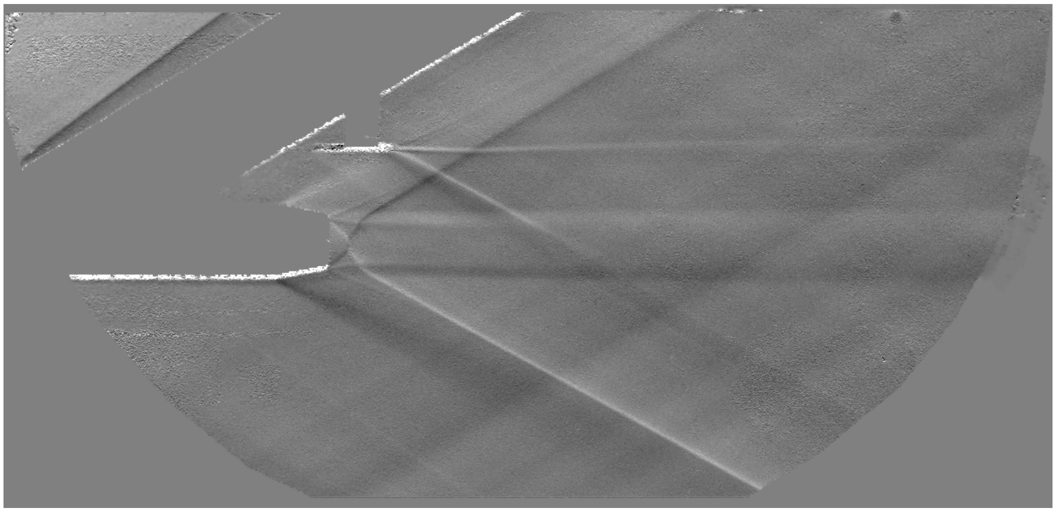

(a) Over-Expanded nozzle, $NPR = 4$.

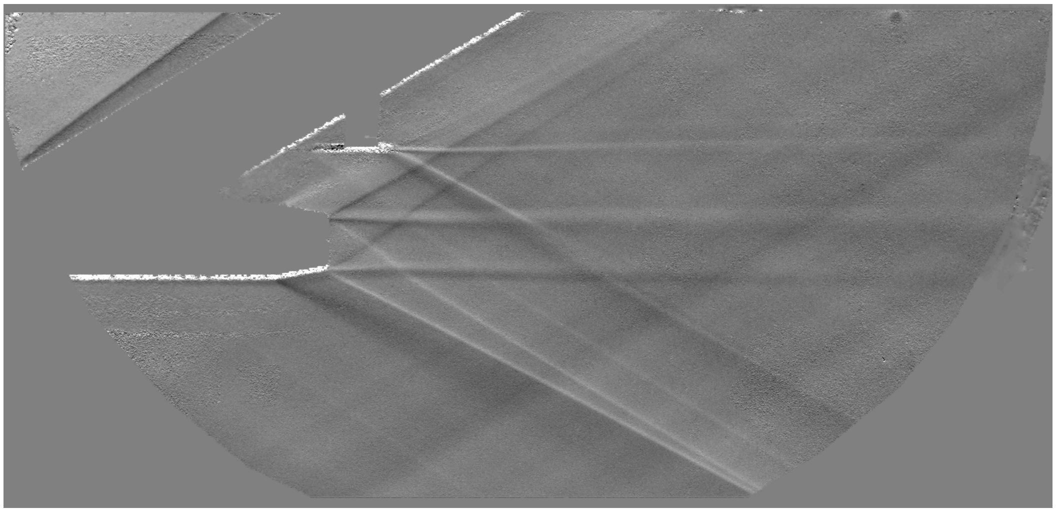

(b) On-Design nozzle, $NPR = 8$.

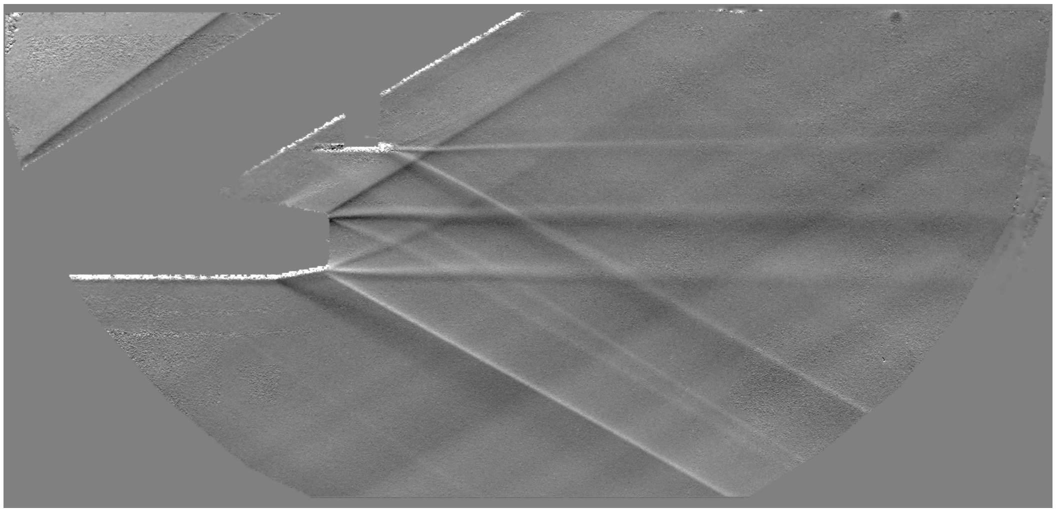

(c) Under-Expanded nozzle, $NPR = 14$.

Figure 7. Biconvex tail interaction at Mach 2, $\alpha = 0°$. Nozzle pressure ratio NPR increasing from top.

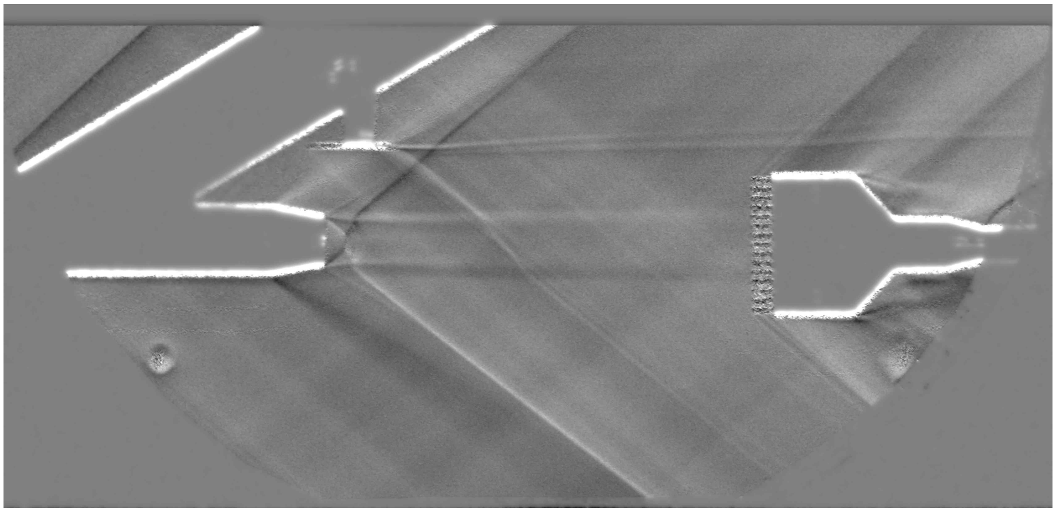

(a) Over-Expanded nozzle, $NPR = 4$.

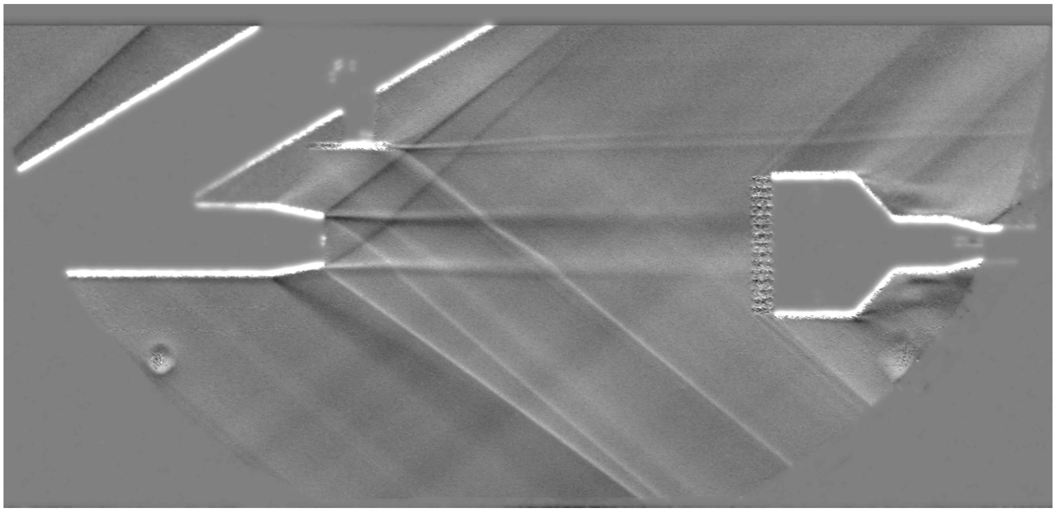

(b) On-Design nozzle, $NPR = 8$.

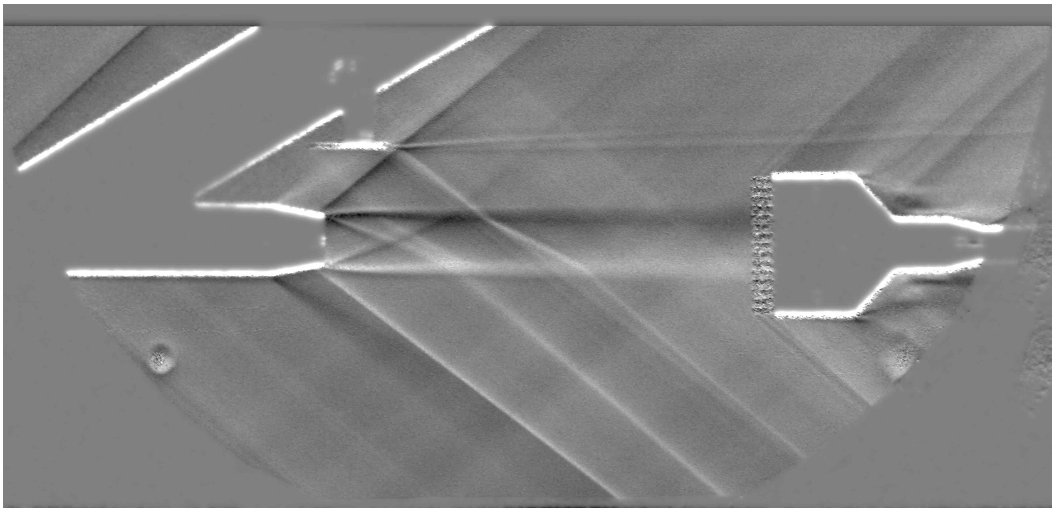

(c) Under-Expanded nozzle, $NPR = 14$.

Figure 8. Biconvex tail interaction at Mach 1.6, $\alpha = 0°$. Nozzle pressure ratio NPR increasing from top.

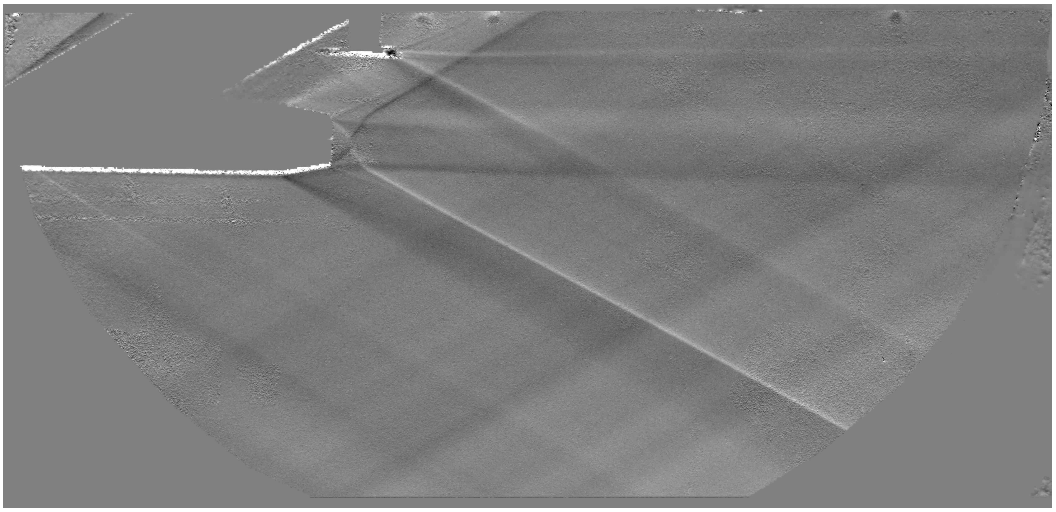

(a) Over-Expanded nozzle, $NPR = 4$.

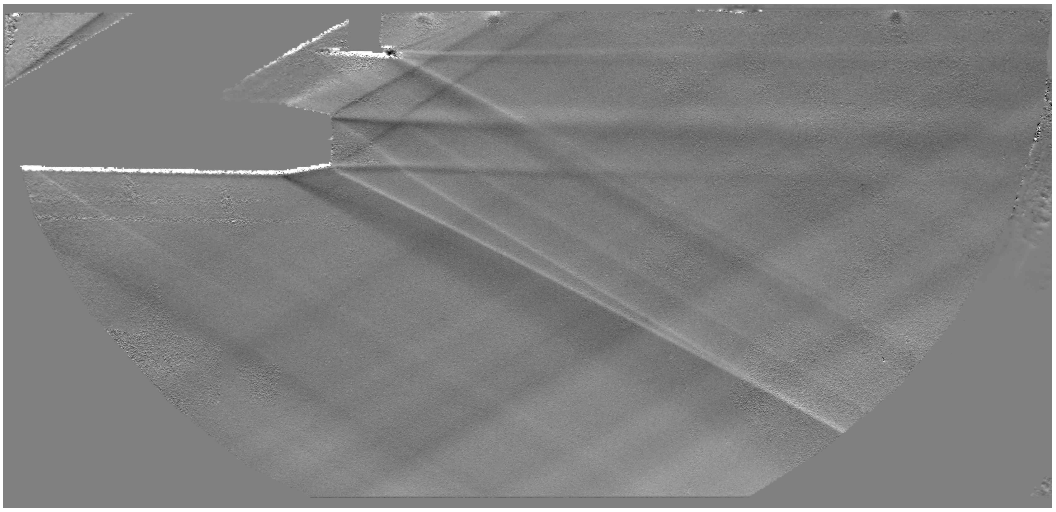

(b) On-Design nozzle, $NPR = 8$.

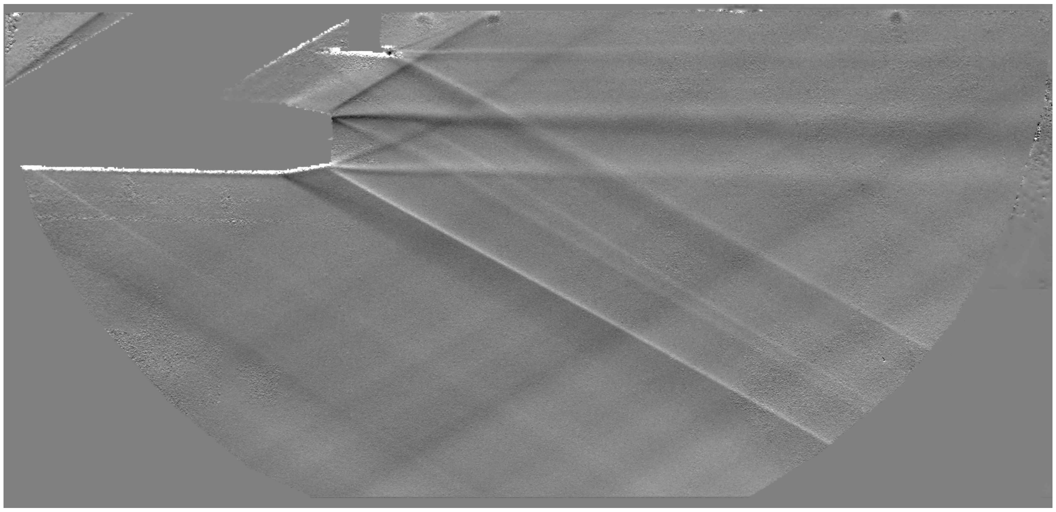

(c) Under-Expanded nozzle, $NPR = 14$.

Figure 9. Biconvex tail interaction at Mach 2, $\alpha = 1°$. Nozzle pressure ratio NPR increasing from top.

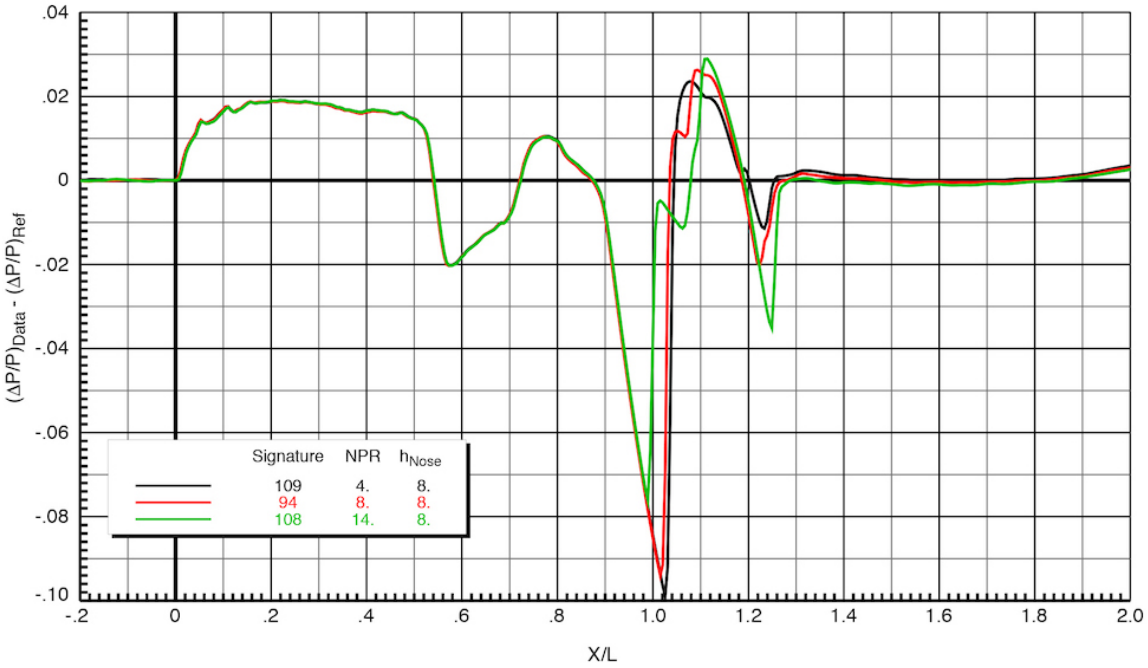

(a) Biconvex tail Mach 2 pressure signatures.

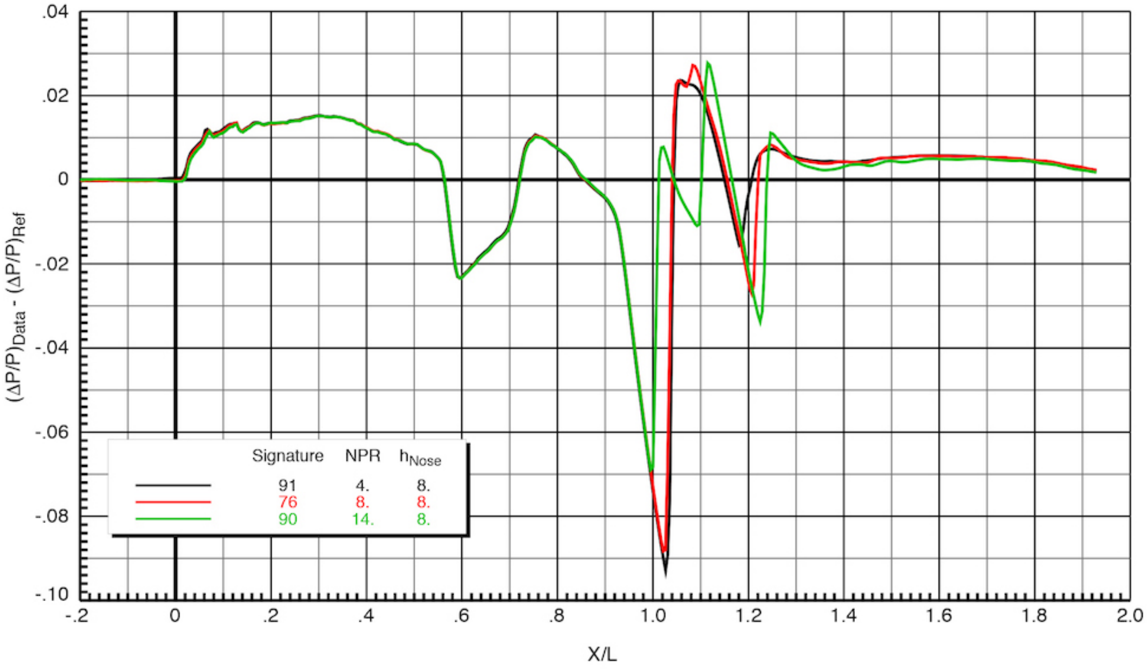

(b) Biconvex tail Mach 1.6 pressure signatures.

Figure 10. Near-field pressure signatures for the biconvex tail at $\alpha = 0$ for NPR 4, 8, and 14. Nozzle body tip located 8 in. above pressure rail.

C. 25-D Tail Interaction

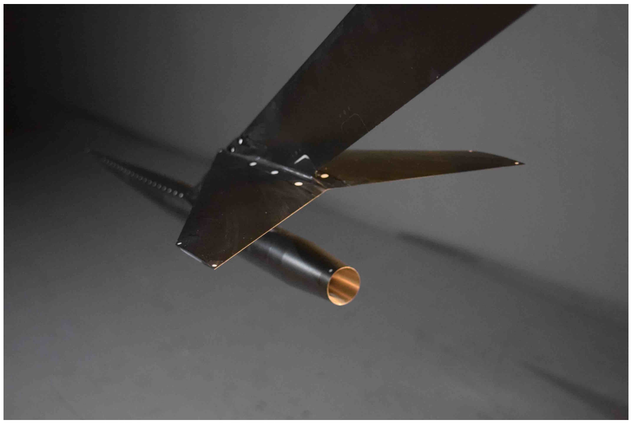

Figure 11. The 25-D tail model installed in the test section.

The large tail model tested is shown in figure 11. This model, termed 25-D, is derived from the NASA Langley low-boom flight demonstrator configuration[9] and has a root cord and span of 6.65 and 9.68 in. respectively. Note that the span of this shock-generator is more than fives times the size of the smaller biconvex tail geometry in figure 6 on page 8. The leading edge is swept by 56°, and the trailing edge by 28.9°. The plume/shock interactions with the 25-D tail shock generator are presented for 0° angle of attack α at freestream Mach numbers of 2 and 1.6, and additionally for Mach 1.6 and $\alpha = 1°$, all at Reynolds numbers of 3.5x10^6/ft. Pressure plots are compared for the 0° α test cases, but data were only recorded at NPR values of 8 and 14 – pressure data were not taken at $NPR = 4$ or for $\alpha = 1°$. Significant model motion could be seen in the raw images at all cases tested for the 25-D model. The observed motion was significant, and caused by rotation of the blade strut. This rotation had a noticeable effect on the tail position from image to image. This motion may have a pronounced effect particularly on the wing trailing edge shear layers, as they will be generated at different image locations for each frame. This motion was also apparent from viewing the raw images from the corresponding Optical Angle of Attack measurements in reference.[?] The 25-D tail model is significantly wider than the nozzle diameter; the images therefore capture the structures generated by the tail that pass both through, and on either side of the plume.

1. 25-D Tail $M = 2.0$ Interaction

Figure 12 on page 18 shows the interactions with the 25-D tail and the nozzle at over, ideal, and under-expanded conditions, corresponding to NPR values of 4, 8 and 14 respectively. NPR is increasing from top to bottom. The nozzle flow structures prior to the plume interaction (above the upper jet boundary) remain the same as in the previous section for the same Mach number as shown in figure 7 on page 11, although the outer nozzle expansion and shock structures have moved downstream due to the longer nozzle used in this configuration. The much larger chord an span of the 25-D tail account for the significantly different flowfields than those of the smaller biconvex tail in figure 7 on page 11. Expansion fans can be seen from both the upper (most noticeably upstream of the strut) and lower convex model surfaces. The plume is initially deflected upward at all values of NPR. This is due to the convex lower surface of the tail that create a series of expansion waves, which partially reflect off of the jet boundary as compression waves, turning the flow upward. This family of waves is difficult to see in some of the images – yet its impact on the jet boundary is evident. As NPR increases, the deflection of the plume becomes less severe as plume Mach number increases. The shocks emanating from both tail trailing edges and the model aft-centerline are visualized clearly at all nozzle operating conditions.

The aft-centerline and tail TE shocks are partially reflected as expansion waves which turn the jet that has been deflected by the tail expansion waves partially back. The transmitted portion of the waves steepen through jet; this steepening becomes more pronounced with increasing NPR as the nozzle exit Mach number increases. Both the aft-centerline and tail shocks slightly steepen as they pass through the plume. This effect is more pronounced for the aft-centerline shock. As with the Mach 2 biconvex tail interaction in figure 7 on page 11, the decrease in wave angle through the plume is not severe relative the wave angle in the freestream. Passage of these shocks through the lower plume boundary appears to be obscured by the three-dimensional nature of the flow, and by the portions of the waves that travel on either side (but not through) the jet plume. Seemingly distinct wakes emanate from each aft wing tip. These shear layers appear to grow as they convect downstream from the model. Note than none of the shock or expansion waves reflecting upward from the jet boundary appear to persist either long enough, or strong enough, to interfere with the wake from the 25-D tail trailing edge wings. The overall trend of the interaction length scale is again an increase with NPR, and still due to the nozzle lower lip shock moving upstream with increasing plume Mach number.

The expansion fans and nozzle lip shocks are clearly discernible in the images at all values of NPR, and their changes with plume exit Mach number are consistent with the biconvex tail interaction in figure 7 on page 11, although these structures have moved further downstream due to the longer nozzle used in the 25-D configuration. Also affected by the longer nozzle is the increased distance between the boat tail expansion and nozzle lower lip shocks. Finally, note that for the under-expanded and nearly ideal operating conditions in figures 7 on page 11 and 12 on page 18, the distance between the nozzle lower lip shocks and transmitted shocks below the lower plume boundary have increased with the 25-D configuration.

The shock from the tail model aft-centerline is located further downstream in the plume as NPR increases. The distance between this shock and the trailing edge shocks seems to be more tightly grouped as they transmit through the lower plume shear layer. This is due to the decrease in the centerline shock wave angle (with increasing NPR) that moves the point on the lower jet boundary where the shock is transmitted. The behavior of the TE shocks for this model in particular is difficult to discern, it does not seem to change location with increased NPR. However, there are significant portions of the shocks that pass outside of the plume in the image due to the large span of the model. This, along with three-dimensionality of the flow, may be contributing to a partial obscuring of the trailing edge shocks in this region, making this portion of the interaction difficult to interpret. It would appear that the effect of decrease in shock angle as it is transmitted through the plume is more pronounced than the biconvex case at the same freestream Mach number. Finally, it appears that the interaction length scale is larger than that of the biconvex tail at all NPR values, this is due to both the longer nozzle and larger root chord of the model.

2. *25-D Tail* $M = 1.6$ *Interaction: Effects of freestream Mach number*

The 25-D shock generator at a freestream Mach number of 1.6 and α of 0°is shown in figure 13 on page 19. Both the the plume structure flow structure and the structures from the shock generator remain largely unchanged from the Mach 2 freestream case as shown in figure 13 on page 19. The entire shock structure, and hence it's length scale, has shifted upstream due to the increased shock angles with decreased freestream Mach number as expected, and as observed with Mach number decrease in the biconvex tail interaction. Comparing figures 13 on page 19 and 12 on page 18, it appears that the interaction length scale has contracted with Mach number.

The shock angles from the nozzle outer lip have steepened due to the decreased freestream Mach number. The interaction of the shock structures through the plume has shifted upstream, closer to the nozzle exit. The angles at which the shock generator structure pass through the shock appear to be the same as their higher Mach number counterparts since the nozzle plume Mach number has not changed, although the relative change in angle as they pass through the plume has steepened. The shocks that pass on either side of the plume, and through the lower shear layer are steeper, and closer upstream to the nozzle shocks for all cases as compared to the higher Mach number scenario in figure 12 on page 18.

A distinct difference between the Mach 1.6 and 2 case is the plume deflection. At all nozzle exit Mach numbers, the plume deflection caused by the shock generator is smaller. This decrease in nozzle plume deflection is due to the weaker shock and expansion waves from the tail at the lower freestream Mach number, which partially reflect from the upper shear layer and turn the flow. The shear layers emanating from the tail trailing edges appear to be deflected here; a flow feature that was not evident at Mach 2 freestream in figure 12 on page 18. The steeper outer nozzle shocks are located closer to the tail trailing edges, and there is a slight possibility of shock impingement on the lower tail surface. However, there is no evidence of a reflection, so this may be due to the three-dimensionality of the flow, or an optical effect of the camera viewing angle.

3. *25-D Tail* $M = 1.6$*,* $\alpha = 1°$ *Interaction*

The 25° tail at Mach 2, angle of attack α of 0° is shown in figure 14 on page 20. As with the biconvex case at 0° α, there is no significant difference in flow structure for a small increase in α. The upper nozzle lip shock appears to near impingement on the tail lower trailing edge surface, although again there is no evidence of shock reflection to substantiate this observation. Sight plume deflection is apparent as in the corresponding $\alpha = 0°$ case, although the relative deflection is difficult to discern due to the angle of attack. One interesting observation can be made regarding the on-design $NPR = 8$ case: the nozzle lower and transmitted nozzle inner lip shocks do not coalesce in the near field as was revealed for the biconvex tail at angle of attack. Pressure signatures were acquired at larger angle of attack, and are presented in reference[1]

4. Pressure Signatures

Figure 15 on page 21 presents the near field pressure signatures for the Mach 2 and 1.6 freestream cases at zero-degree angle of attack α. For these runs, pressure signature measurements were only performed at nozzle NPR of 4 and 8 – the signatures for the over-expanded cases were not measured. The regions in figures 19(a) on page 26 and 15(b) on page 21 ahead of $x/L \approx .95$ are due to the nose shock, nozzle body expansion and blade strut respectively. The signatures of this region do not change with NPR. There is difference in shape of the signature associated with the blade strut between the two freestream Mach number for which we do not have an explanation. The steepest drop in pressure is due to the nozzle boat tail expansion – the sharp pressure rise which follows this in both figures at $x/L \approx 1.0$ is caused by the nozzle lower lip shock. It is interesting that the location of this shock does not change with NPR, as was seen in clearly in the images. Even more striking is that this structure does not move upstream with decreased freestream Mach number as was also observed in the images. It is observed however, in both instances, that the strength of the lower lip shock becomes stronger with increased NPR, as was noted by the steepening of this wave angle with increased NPR. Since this pressure rise is so large, it may be indicative of a coalescing of this shock with the 25-D leading edge shock – this shock is difficult to see, but must be present – and complicated by the fact that it needs to pass around the nozzle body, which would certainly effect its geometry. The large drop in pressure from $x/L \approx 1.05$ to 1.4 in both figures 19(a) on page 26 and 15(b) on page 21 denote the expansion from the lower model surface. This large expansion surface, coupled with three-dimensional shocks from the leading and twin trailing edges, as well as the centerline shock make the finer features in the signature difficult to interpret with any certainty. What is clear is that the interaction length scale increases with NPR for a given freestream Mach number, but decreases with lower freestream Mach number and fixed NPR.

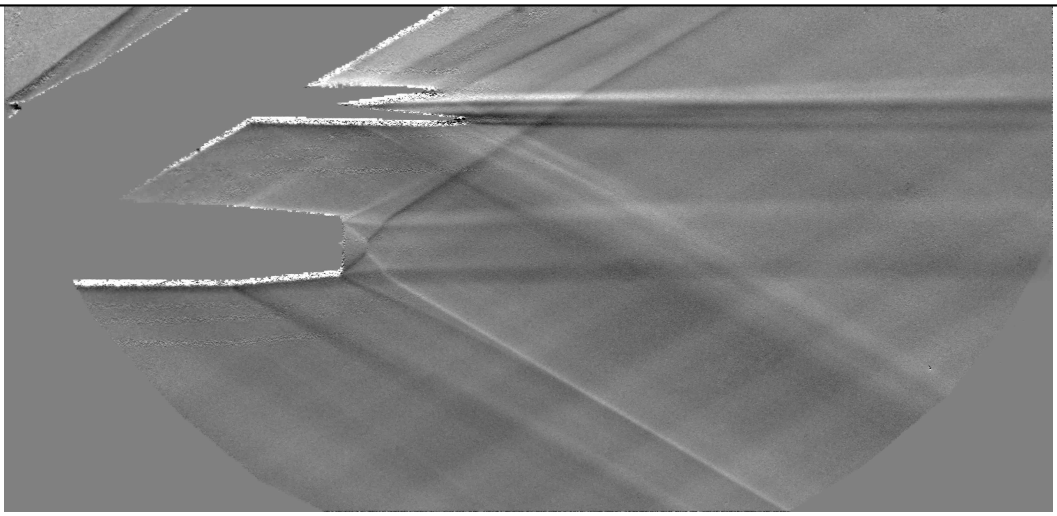

(a) Over-Expanded nozzle, $NPR = 4$.

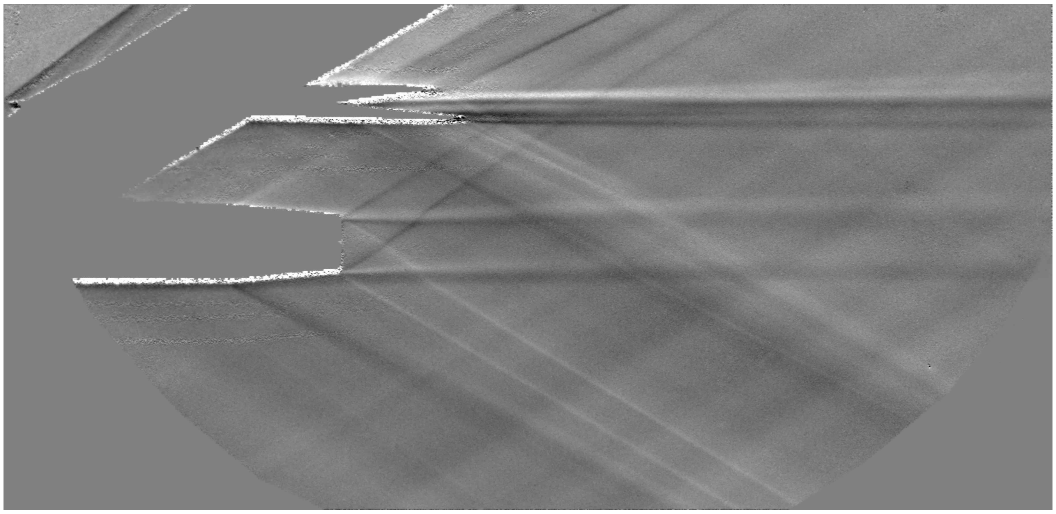

(b) On-Design nozzle, $NPR = 8$.

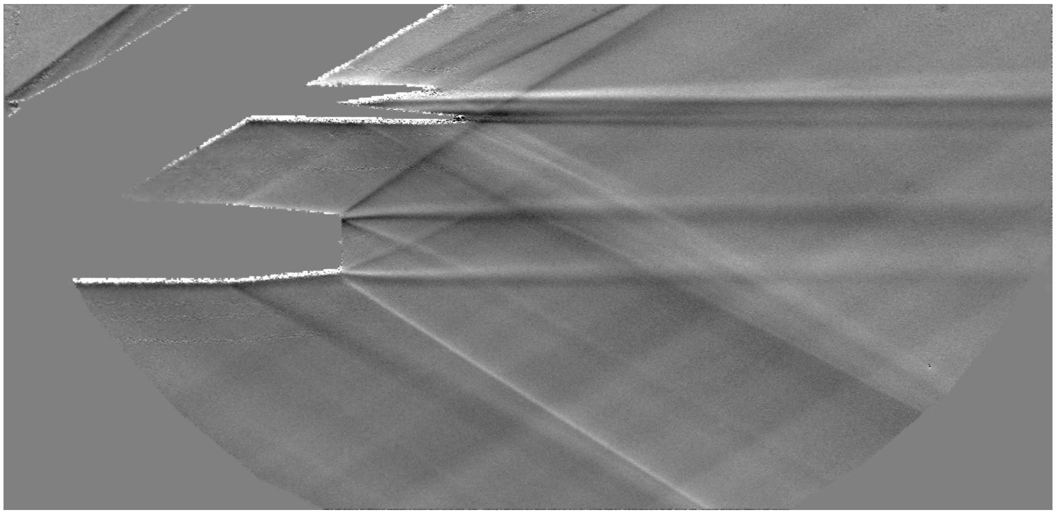

(c) Under-Expanded nozzle, $NPR = 14$.

Figure 12. 25-D tail interaction at Mach 2, $\alpha = 0°$**. Nozzle pressure ratio (**NPR**) increasing from top.**

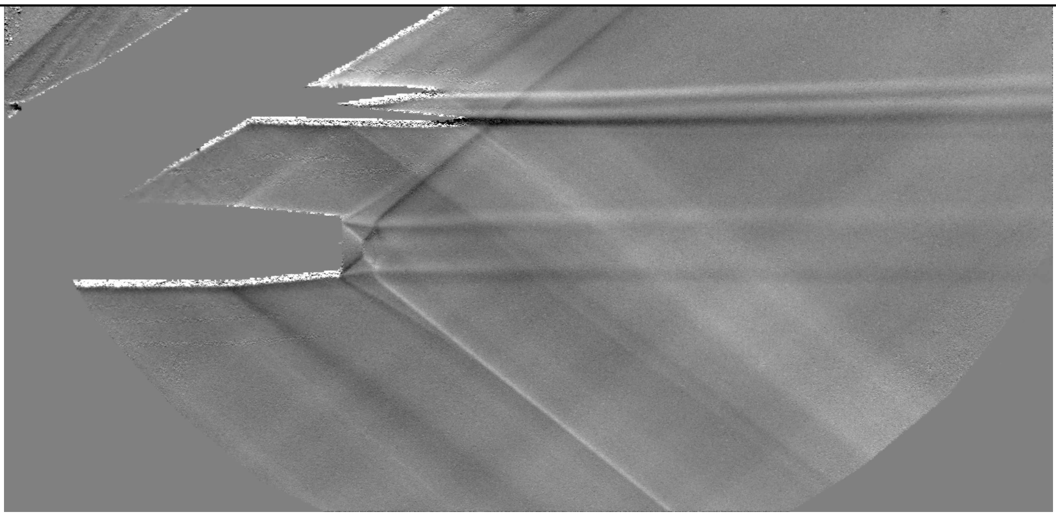

(a) Over-Expanded nozzle, $NPR = 4$.

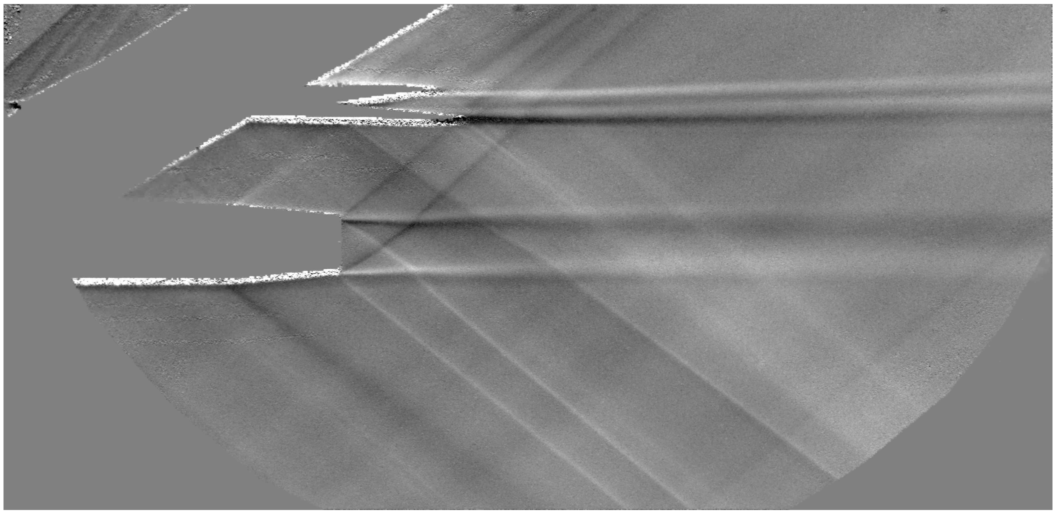

(b) On-Design nozzle, $NPR = 8$.

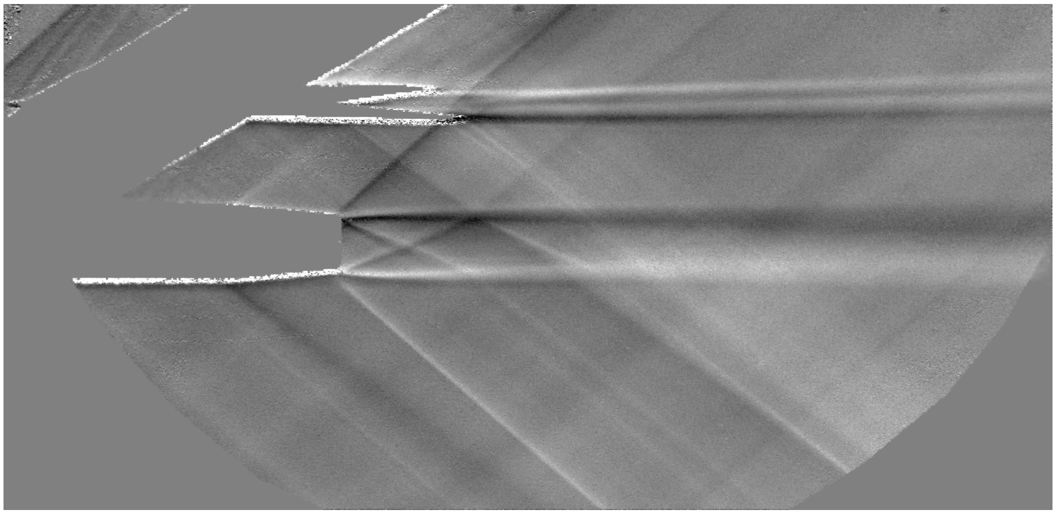

(c) Under-Expanded nozzle, $NPR = 14$.

Figure 13. 25-D tail interaction at Mach 1.6 $\alpha = 0°$. Nozzle pressure ratio (NPR) increasing from top.

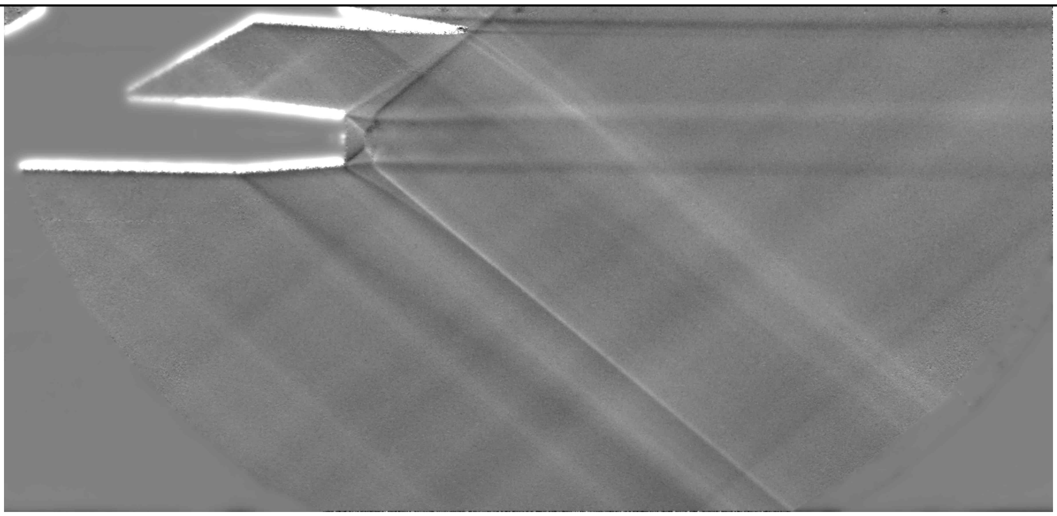

(a) Over-Expanded nozzle, $NPR = 4$.

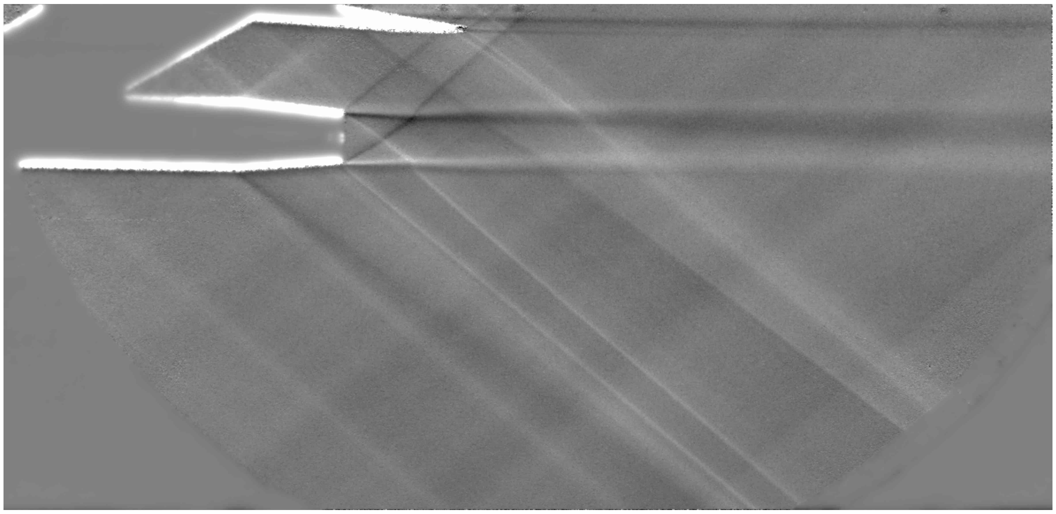

(b) On-Design nozzle, $NPR = 8$.

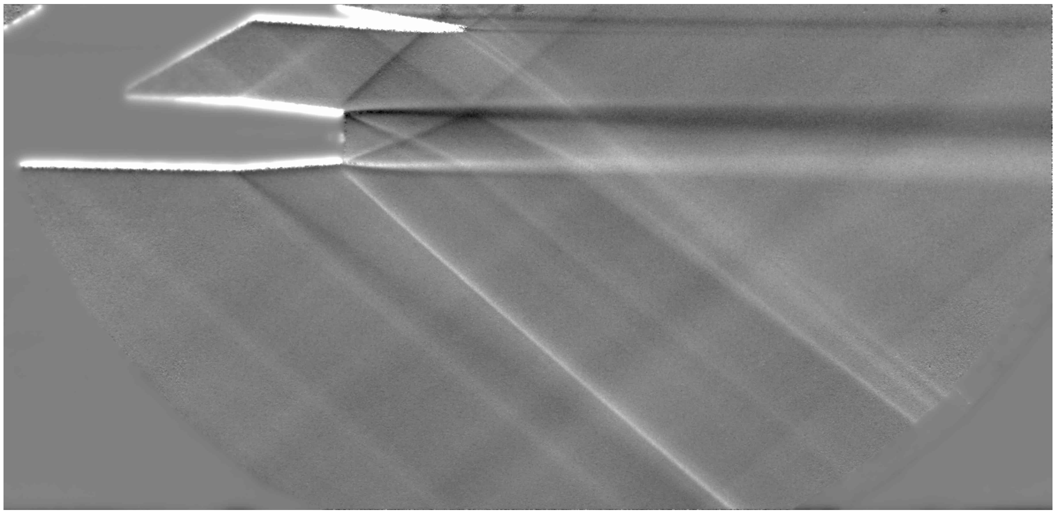

(c) Under-Expanded nozzle, $NPR = 14$.

Figure 14. 25-D tail interaction at Mach 1.6 $\alpha = 1°$. Nozzle pressure ratio (NPR) increasing from top.

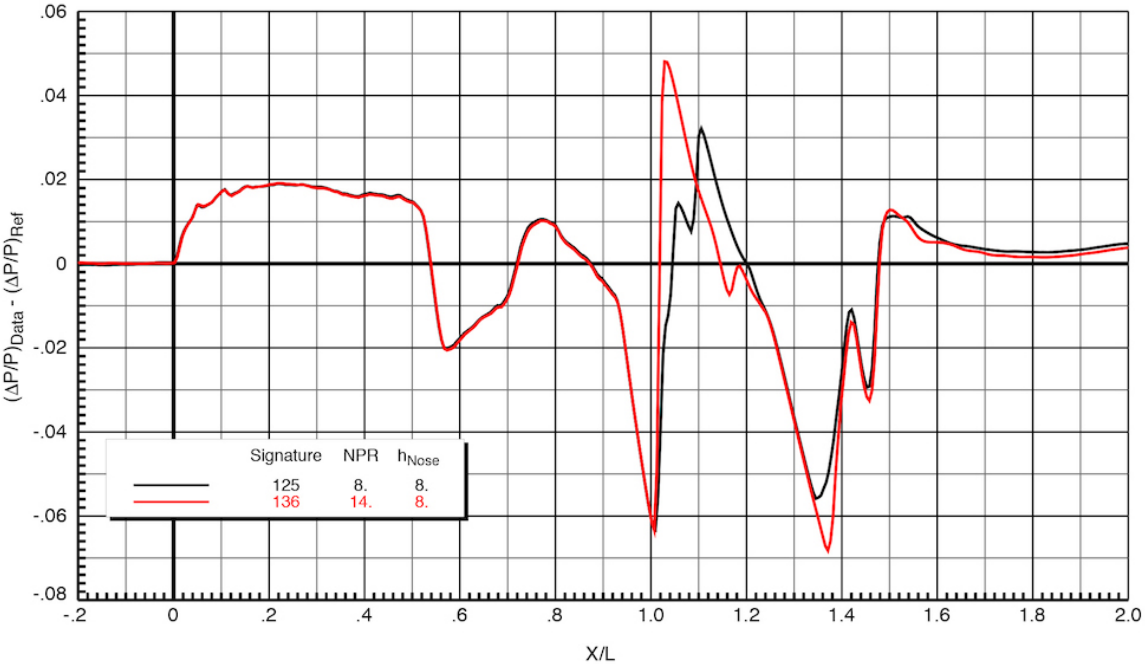

(a) 25-D tail Mach 2 pressure signatures.

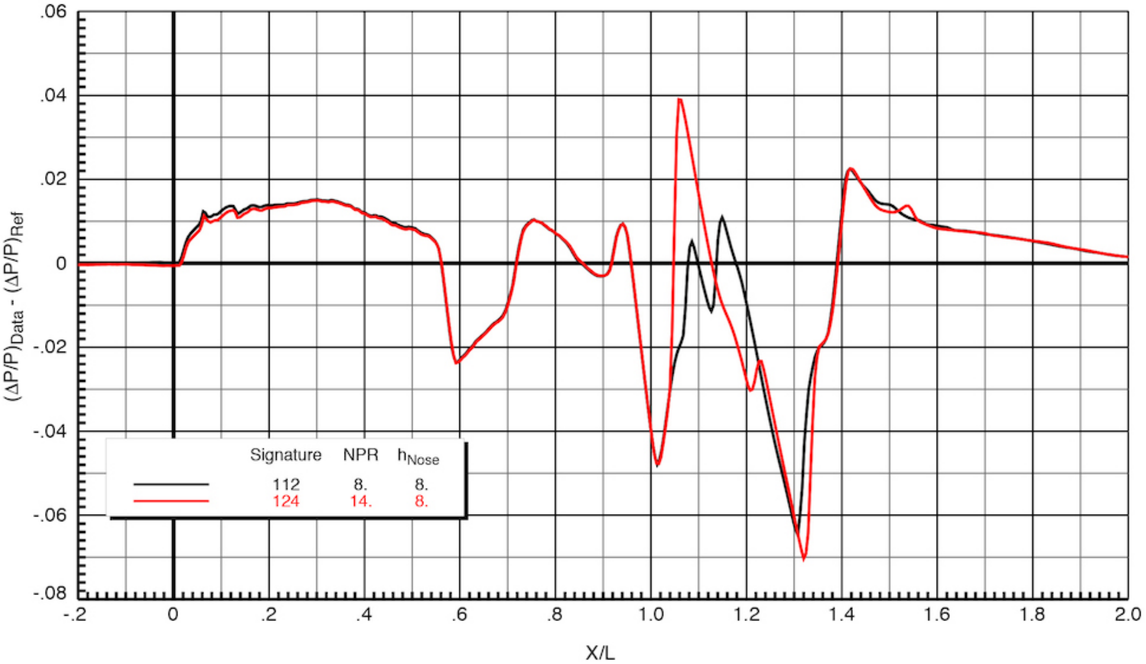

(b) 25-D tail Mach 1.6 pressure signatures.

Figure 15. Near field pressure signatures for the 25-D tail at $\alpha = 0$ for NPR 8, and 14. Nozzle body tip located 8 in. above pressure rail.

D. Aft Deck Interaction

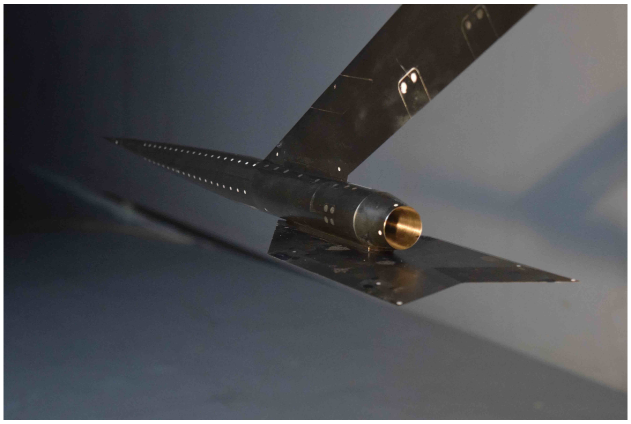

Figure 16. The Aft deck shield model installed in the test section.

The aft-deck shock generator was designed to resemble an extended aft-fuselage section between wing surfaces, that provide nozzle shielding below the engine nacelle for mitigation of sonic boom – specifically to keep the lower nozzle lip shock from propagating downward and contributing to the pressure signature. Shown in figure 16, the aft-deck model has a root chord of 9.56 in., and a span of 5 in. The leading and trailing edges are swept by 60° and 26°. Results for the aft-deck plume/shock interaction are presented for Mach 2 with a Reynolds number of 3.5x10^5 at angles of attack α of 0 and 1°. Pressure signatures are presented for the $\alpha = 0$ case. Durston *et al.*[1] present additional results for this configuration including effects of roll and angle of attack. Model motion was apparent at this configuration from viewing the raw images, the rotation of the blade strut resulted in a "thickening" of the aft-deck model surface appearing in the raw data. Therefore, flow structures on the model surface such as the boundary layer, were not captured in the schlieren images.

1. Aft-deck $M = 2$ Interaction

Figure 17 on page 24 shows the schlieren image results for the aft-deck at Mach 2 freestream again at over, ideal and over-expanded operating conditions. NPR is increasing from top to bottom. The nozzle plume structures are markedly different from those viewed in the tail geometry interactions, as downward propagating inner lip waves now impinge on the plate surface and reflect. The locations where the nozzle lip shocks impact the aft-deck are likely to be regions of increased localized heating. As far as these impingements resulting in any shock wave/boundary-layer interactions, image resolution in these areas are insufficient to draw conclusions. Noticeably lacking from all images is the nozzle lower lip shock–it has been diverted upward by the aft-deck surface and does not contribute to the ground pressure signature as designed. Downward directed plate LE shocks are apparent below the aft-deck surface and do not change with NPR. These LE shocks are likely to influence the pressure signatures; however, the aft-deck will be integrated with the upper aft fuselage section on an aircraft, so these additional shocks will not occur on a vehicle configuration. At all values of NPR, a thick wake emanates from the aft-deck trailing edge.

For the over-expanded case in figure 17(a) on page 24, the downward propagating nozzle inner lip shock reflects from the flat plate appearing to transmit through the upper plume boundary, and seems to terminate in a normal shock approximately one nozzle diameter downstream of the exit. Expansion waves are evident from the downward directed plume downstream of the nozzle exit plane. The expansion fans emanating from the upper trailing edge coalesce with the centerline and aft-deck TE tip shocks, which turn the nozzle plume parallel to the wall.

The ideal ($NPR = 8$) plume appears again to be slightly over-expanded and has increased in height, and the impinging nozzle inner lip shock has moved downstream. A nozzle outer lip shock is now evident, and the aft-deck TE shock angle may have decreased with the increased NPR. The expansion from the aft-deck trailing edge also decreases in angle with increased plume Mach number. The downward directed centerline and TE shocks from the aft-deck do not appear to have moved upstream with increased NPR. Similar trends are evident in figure **??** on page ??, where the leading expansion wave from the aft-deck has decreased in angle and the plume has again thickened with increased NPR. The point where the reflected shock from the aft-deck surface turns the plume parallel to the wall has shifted slightly downstream. A significant difference in the under-expanded case is what appears to be a coalescing of the lower surface centerline and TE shocks – they are no longer as distinct as they were at lower plume exit Mach numbers. The overall trend of the interaction length scale is difficult to determine in the image, at least below the aft-deck aside from the TE shock coalescence. Above the aft-deck however, the length scale is decreasing with NPR.

2. *Aft-deck $M = 2$, $\alpha = 1°$ Interaction*

The aft-deck interactions at Mach 2 and $\alpha = 1°$ are presented in figure 18 on page 25. Again, there are no significant flow difference, and pressure signature measurements are lacking for this case. Durston *et al.*[?] present signatures for higher angles of attack. The pressure signatures are likely to differ significantly, as the aft-deck should behave as a lifting surface at angle of attack.

3. *Pressure signatures*

Pressure signatures for the aft-deck interaction are shown in figure 19 on page 26 at a freestream Mach number of 2 and angle of attack $\alpha = 0°$. Nozzle pressure ratios are increasing from top. The highest pressure rise occurs at $x/L \approx .85$ at all NPR conditions. This is due to the aft-deck leading edge centerline and wingtip shocks, and does not change with NPR. As discussed previously, the aft-deck geometry would be integrated into the upper portion of the fuselage and this shock would not be present in an aircraft configuration. The immediate expansion past this point is an effect of the three-dimensionality of the flowfield. There are two distinct shocks for the over-expanded ($NPR = 4$) and ideally expanded ($NPR = 8$) cases. These are caused by the aft-deck TE centerline and TE wingtip shocks. For the under-expanded operation at $NPR = 14$, these TE shocks seemed to have coalesced into a strong shock.

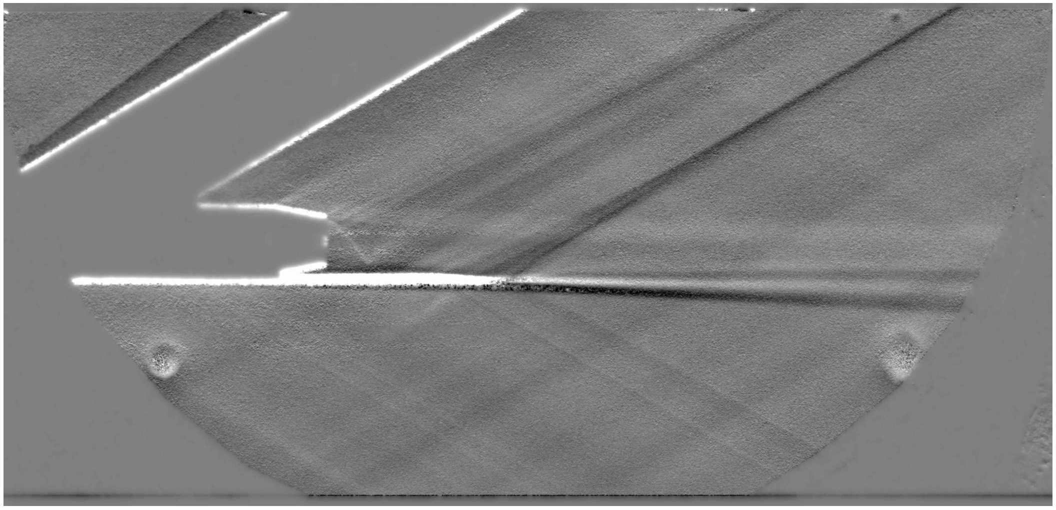

(a) Over-Expanded nozzle, $NPR = 4$.

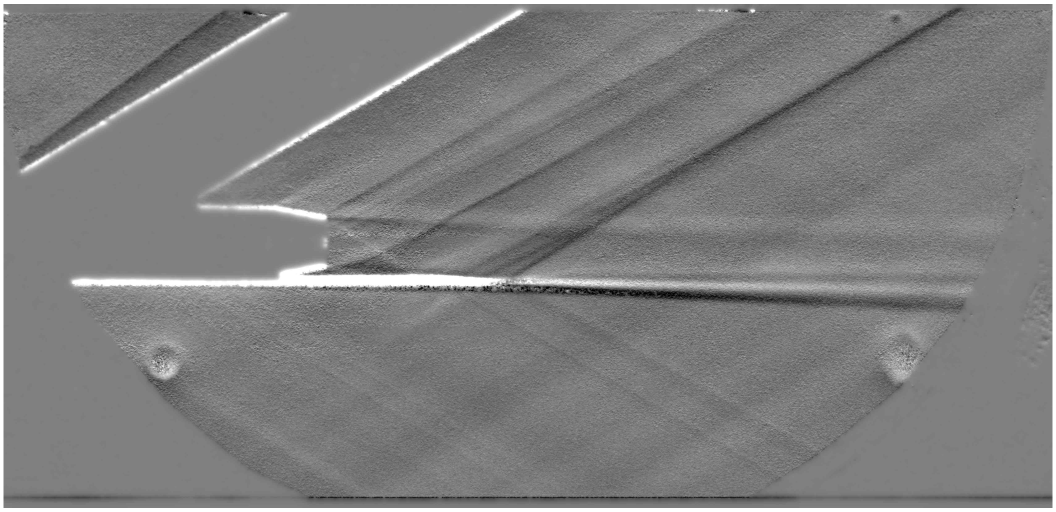

(b) On-Design nozzle, $NPR = 8$.

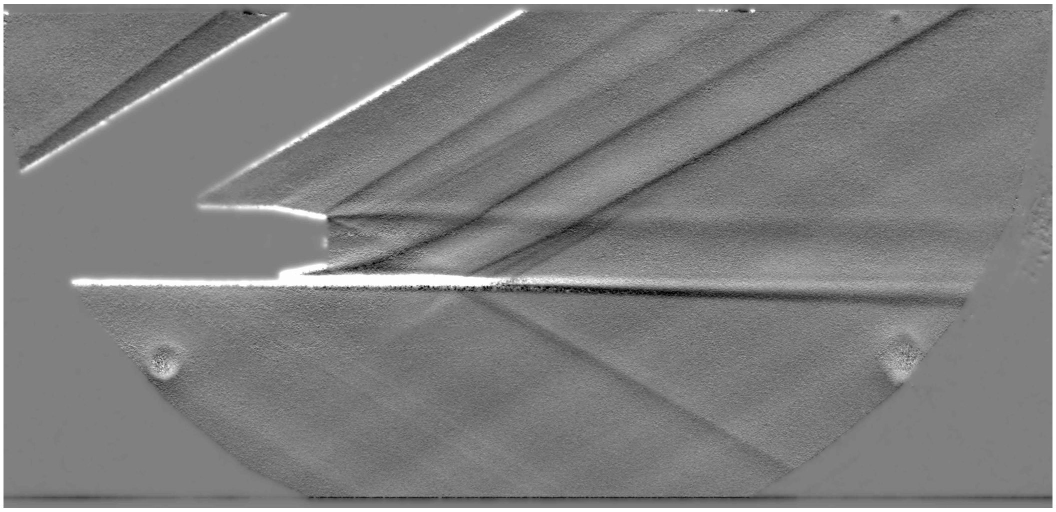

(c) Under-Expanded nozzle, $NPR = 14$.

Figure 17. Aft-deck interaction at Mach 2 $\alpha = 0°$. Nozzle pressure ratio (NPR) increasing from top.

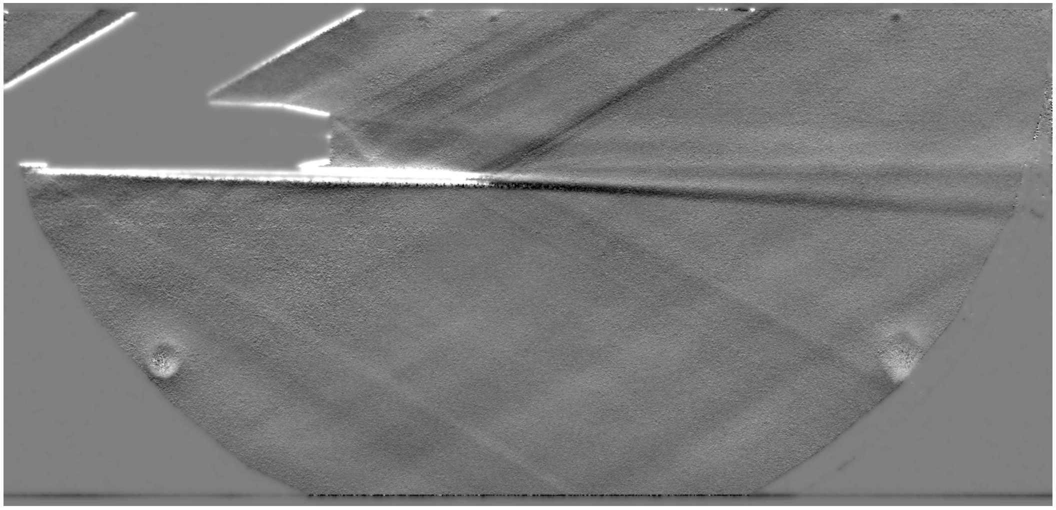

(a) Over-Expanded nozzle, $NPR = 4$.

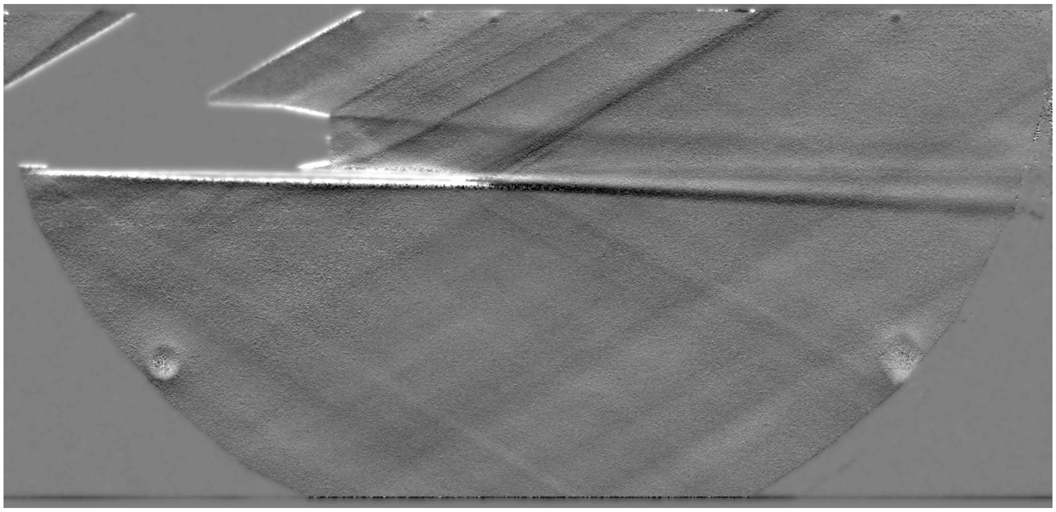

(b) On-Design nozzle, $NPR = 8$.

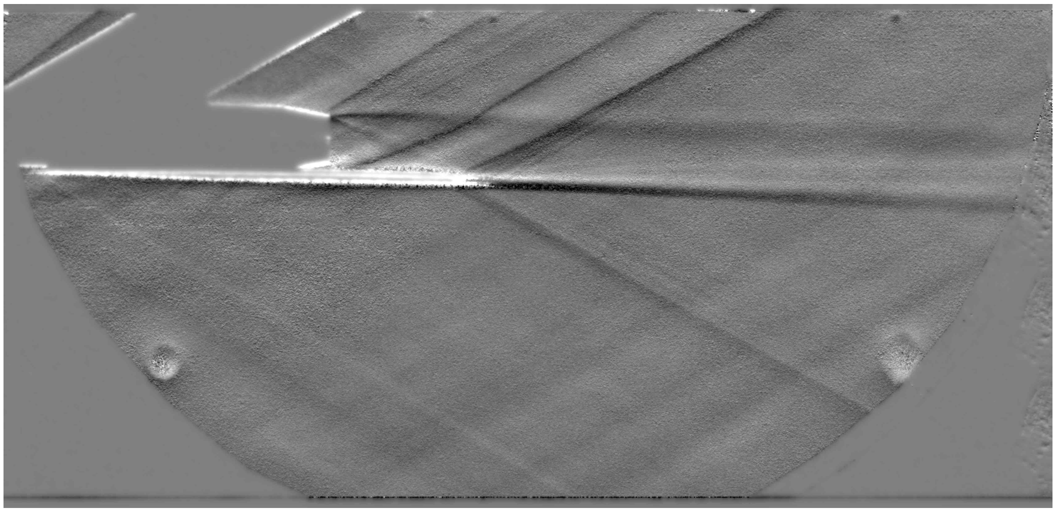

(c) Under-Expanded nozzle, $NPR = 14$.

Figure 18. Aft-deck interaction at Mach 2 $\alpha = 1°$. Nozzle pressure ratio (NPR) increasing from top.

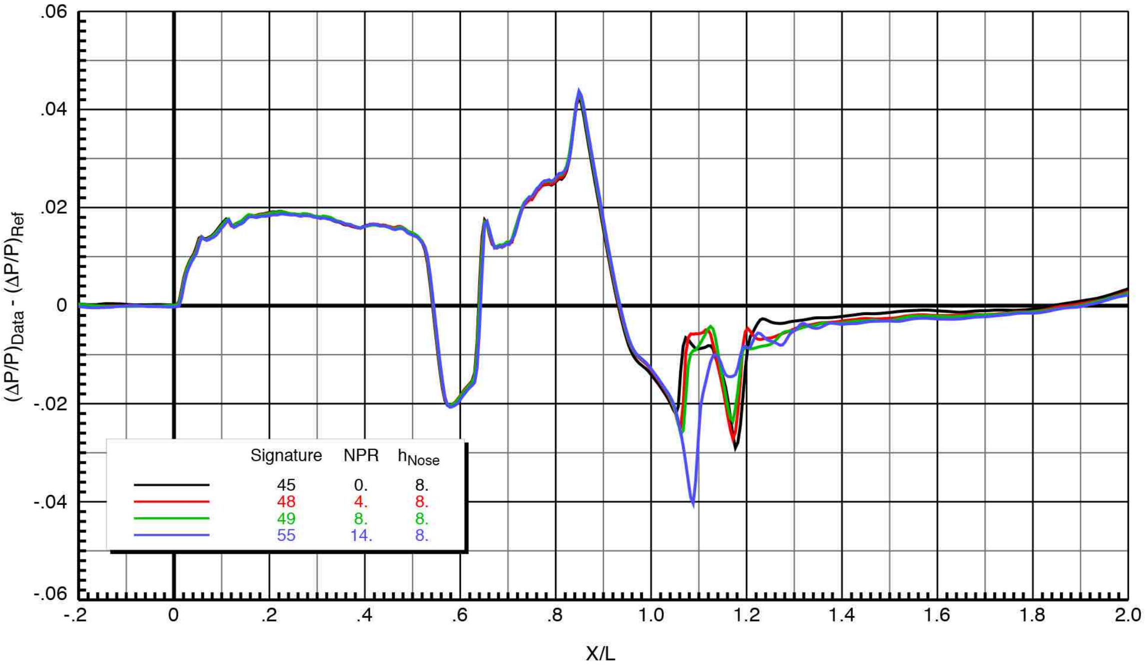

(a) Aft-deck Mach 2 pressure signatures.

Figure 19. Near-field pressure signatures for the aft-deck at $\alpha = 0$. Nozzle body tip located 8 in. above pressure rail.

VII. Conclusions

Optical flow was used to generate background oriented schlieren images for the NASA Ames shock/plume interaction tests. This is the first use of optical flow in a production test at the NASA Ames UPWT, as opposed to the standard normalized cross correlation method, to produce background oriented schlieren images. Optical flow provided images with increased resolution and flow detail as compared to those produced with cross correlation. The highly detailed interaction images, together with pressure signatures in the near field allowed for interpretation of the plume/shock interaction flowfields for select shock-generating geometries. Images for all shock-generating configurations allowed clear identification of the plume flow structures associated with over, ideal, and under-expanded nozzle operation.

For all tail model plume/shock interactions presented here, shocks from the tail models decrease in angle as they transmit through the plume, and continue to do so with increasing plume Mach number and NPR. The nozzle outer lip shocks steepen and move upstream with increasing plume exit Mach number (NPR) at a fixed freestream Mach number, and decreased freestream Mach number for a fixed value of NPR. The effects of upstream shock motion caused a decrease in the interaction length scale in the near field – this is attributed largely to the increase in angle of the nozzle lower lip shock with increased NPR, and the additional steepening associated with decreased freestream Mach number. The biconvex tail did not seem to deflect the plume, but the large 25-D tail caused significant deflection at lower NPRs and high freestream Mach number. The 25-D interaction length scale was also larger than that of the biconvex tail, again due to the larger model size. At larger values of NPR, it is possible that the nozzle shocks may impinge on the lower surface of the 25-D tail, although this is inconclusive as a reflected shock was not observed in the images, nor in the pressure signatures. There were no noticeable changes in the interaction structures at the small angles of attack presented here, and pressure signatures for $\alpha = 1°$ were not available. The effects of angle of attack are considered in reference,[?] where higher values of α and their corresponding pressure signatures are presented.

The aft-deck deflected the downward propagating nozzle lip shock as designed. The nozzle outer lip shock was among the strongest shocks present in the interactions with the tail models, and the nozzle shielding prevents this shock from contributing to the pressure signature. Shocks from the nozzle impinge on the upper aft-deck surface, which may result in regions of increased localized heating. At the under-expanded operating condition for the aft-deck, there is likely a confluence of the model TE shocks which may account for the stronger pressure rise at this case.

Acknowledgments

The authors would like to acknowledge Bron Nelson and Chris Heinze of the NAS at NASA Ames for their considerable guidance during the code development phase of this work. Helpful conversations were had with Professor Andrew Meade of Rice University.

References

[1] Durston, D. A., Cliff, S. E., Denison, M. F., Smith, N. T., Heineck, J. T., Schairer, E. T., Kushner, L. K., Castner, R. S., Elmiligui, A. A., Carter, M. B., Winski, C. S., Shea, P. R., and Blumenthal, B. T., chap. Nozzle Plume/Shock Interaction Sonic Boom Test Results from the NASA Ames 9- by 7-Foot Supersonic Wind Tunnel, AIAA Science and Technology, American Institute of Aeronautics and Astronautics, Janurary 2017.

[2] Durston, D., Elmiligui, A., Cliff, S., Winski, C., Carter, M., and Walker, E., “Experimental and Computational Sonic Boom Assessment of Boeing N+2 Low Boom Models,” Jan. 2015.

[3] Dalziel, S. B., Hughes, G. O., and Sutherland, B. R., “Synthetic schlieren,” *Proc. 8th Int. Symp. on Flow Visualization*, 1998.

[4] Richard, H. and Raffel, M., “Principle and applications of the background oriented schlieren (BOS) method,” *Measurement Science and Technology*, Vol. 12, No. 9, 2001, pp. 1576.

[5] Raffel, M., “Background-oriented schlieren (BOS) techniques,” *Experiments in Fluids*, Vol. 56, No. 3, 2015, pp. 60.

[6] Heineck, J. T., Schairer, E. T., Walker, L., and Kushner, L., “Retroreflective background oriented schlieren (rbos),” *Proceedings of the 14th international symposium on flow visualization (ISFV14), EXCO Daegu, Korea*, 2010.

[7] Horn, B. K. and Schunck, B. G., “Determining optical flow,” *Artificial intelligence*, Vol. 17, No. 1-3, 1981, pp. 185–203.

[8] Cliff, S., “On the Design and Analysis of Low Sonic Boom Configurations,” Nasa conference publication 10133, high speed research: Sonic boom volumes i and ii, presented at the high speed research sonic boom workshop, ames research center, May 1993.

[9] Ordaz, Irian, W. M. and Rallabhandi, S., “Full-Carpet Design of a Low-Boom Demonstrator Concept,” Aiaa paper 2015-2261, 33rd aiaa applied aerodynamics conference dallas, tx, June 2015.